Tectonics®

RESEARCH ARTICLE
10.1029/2022TC007503

Key Points:

- Salt distribution determines the evolution and architecture of a salt-bearing rifted margin incorporated into a fold-and-thrust belt system
- Salt extrusion and erosion lead to an underestimation of the original amount of salt which may compromise structural restorations
- Analog modeling results support the salt-influenced evolutionary model for the Northern Calcareous Alps

Correspondence to:
P. Santolaria,
p.santolaria.otin@ub.edu

Citation:
Santolaria, P., Granado, P., Wilson, E. P., de Matteis, M., Ferrer, O., Strauss, P., et al. (2022). From salt-bearing rifted margins to fold-and-thrust belts. Insights from analog modeling and Northern Calcareous Alps case study. *Tectonics*, *41*, e2022TC007503. https://doi.org/10.1029/2022TC007503

Received 20 JUL 2022
Accepted 9 NOV 2022

Author Contributions:
Conceptualization: P. Santolaria, P. Granado, J. A. Muñoz
Formal analysis: P. Santolaria, P. Granado, E. P. Wilson, M. de Matteis
Funding acquisition: P. Granado, J. A. Muñoz
Investigation: P. Santolaria, P. Granado, J. A. Muñoz
Methodology: P. Santolaria, P. Granado
Project Administration: P. Granado
Resources: O. Ferrer
Supervision: J. A. Muñoz
Writing – original draft: P. Santolaria, P. Granado
Writing – review & editing: P. Santolaria, P. Granado, E. P. Wilson, M. de Matteis, O. Ferrer, P. Strauss, K. Pelz, M. König, A. E. Oteleanu, E. Roca, J. A. Muñoz

From Salt-Bearing Rifted Margins to Fold-And-Thrust Belts. Insights From Analog Modeling and Northern Calcareous Alps Case Study

P. Santolaria[1], P. Granado[1], E. P. Wilson[1], M. de Matteis[1], O. Ferrer[1], P. Strauss[2], K. Pelz[2], M. König[2], A. E. Oteleanu[2], E. Roca[1], and J. A. Muñoz[1]

[1]Departament de Dinàmica de la Terra i de L'Oceà, Facultat de Ciències de la Terra, Institut de Recerca Geomodels, Universitat de Barcelona (UB), Barcelona, Spain, [2]OMV Exploration and Production GmbH, Vienna, Austria

Abstract Analog modeling is used to study the role played by the inherited salt-sediment architecture of a salt-bearing rifted margin, developed by minibasin downbuilding and margin-scale gliding, and then incorporated into a fold-and-thrust belt system influenced by surface processes. Inherited salt bodies localize contractional deformation at different scales and the salt-sediment architecture determines structural styles of fold-and-thrust belts. In our analog models, a large-transport thrust detached along allochthonous model salt (silicone polymer) accumulated in a former distal raft system. And the squeezing of salt walls, together with the tilting of minibasins, accounted for most of the shortening in a salt wall-minibasin province. Shortening and surface processes promote the extrusion and erosion of about 75% of the original model salt. The role played by salt tectonics during the contraction of salt-bearing rifted margins could be underestimated because of the low salt-sediment ratio found in fold-and-thrust belts. Our modeling results are compared with and assist in the interpretation of a section along the Northern Calcareous Alps.

1. Introduction

Salt-influenced fold-and-thrust belts are characterized by intricate structural geometries and salt-sediment interactions. Diagnostic structural geometries associated with these systems include large, overturned panels, large-transport thrust sheets, frequent changes in structural orientations and fold plunges, and contacts either omitting or repeating stratigraphy marked by welds (e.g., Celini et al., 2020; Graham et al., 2012; Granado et al., 2019; Letouzey et al., 1995; McClay et al., 2004; Saura et al., 2016; Strauss et al., 2020) (Figure 1). The main reasons for this are the inherent weakness of salt, the presence of pre-shortening salt structures, and the inherited uneven stratigraphic thickness distribution related to salt-sediment interaction (i.e., the so-called *non-layer cake* stratigraphy). Such inheritance represents a first order factor that controls deformation during contraction (Callot et al., 2012; Ferrer, 2012; Jackson et al., 2011; Moretti et al., 2013; Rowan & Vendeville, 2006; Santolaria, Ferrer, et al., 2021; Santolaria, Granado, et al., 2021). In those salt-bearing rifted margins featuring a late syn-rift to post-rift salt basin, the salt-sediment system evolves by gravitational collapse and by differential loading of sediments leading to salt evacuation and creation of accommodation space (e.g., Brun & Fort, 2004, 2011; Ge et al., 1997; Ge et al., 2020; Granado et al., 2016; Jackson & Hudec, 2017; Peel, 2014; Pichel et al., 2022; Rowan et al., 2012). Resulting geometries include a myriad of salt-bearing structures and sedimentary geometries that are representative of this rifted margin settings and diagnostic of certain controlling mechanism (Brun & Fort, 2004, 2011; Dooley et al., 2017, 2018; Pichel et al., 2021; Rowan, 2020a, 2020b; Rowan et al., 2022; Granado et al., 2022): Rollovers, primary and secondary and minibasins depicting layer, wedge and trough sedimentary sequence geometries (Rowan & Giles, 2022; Rowan & Weimer, 1998), rafts, turtles, and diapirs among others (Figure 1a). These are the potential structural and stratigraphic elements to be subsequently incorporated in contractional systems and so, these templates must be considered when reconstructing the overall geometry of certain fold-and-thrust belts developed from a rifted margin involving salt tectonics.

As a result of shortening and erosion of these salt-bearing rifted systems, salt can flare and be extruded to the actively deforming surface. Salt can also be driven downwards, back into its original source layer as diapirs are shortened, squeezed and shut-off (i.e., Dooley et al., 2009; Granado et al., 2021). Salt extrusion points can be located at the emergent tips of salt-detached thrust sheets (ref. this study; Hudec & Jackson, 2006), or in the crest of growing detachment anticlines (Bonini, 2003; Rowan et al., 2022; Santolaria et al., 2015). Once salt extrudes to the surface, it will interact with sedimentation and erosion, thus its preservation potential is limited by

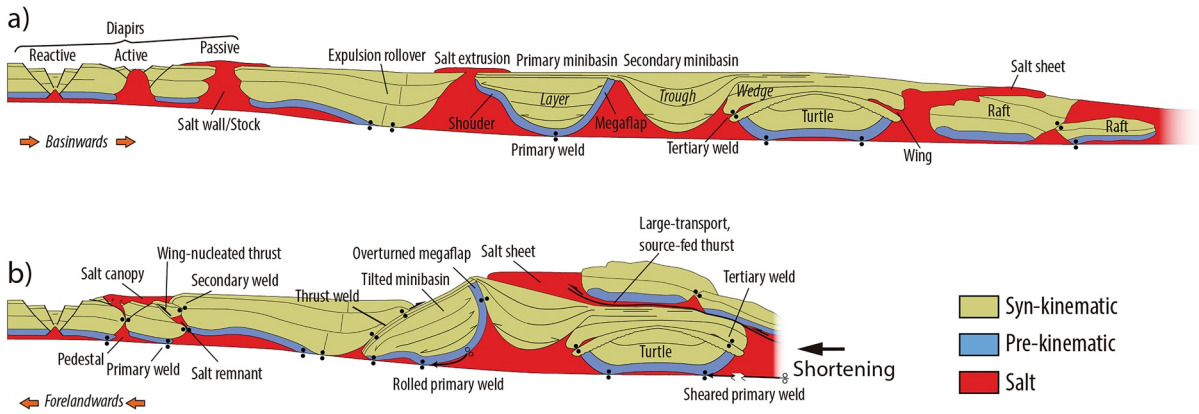

Figure 1. Sketched sections that illustrate a compilation of salt-related structures (regular labels) and sedimentary sequence geometries (italic labels) used throughout the text and occurring in (a) salt-bearing rifted margins and (b) salt-bearing rifted margins involved in fold-and-thrust belts. See Jackson and Hudec (2017) and Granado et al. (2022) for a complete list of terms and definitions.

environmental conditions and the balance between syn-orogenic sedimentation and erosion. World-class examples of thrust-related salt sheets are the Quele sheet in the Kuqa basin (e.g., Li et al., 2014), the Lufilian Arc of the Democratic Republic of Congo (Jackson et al., 2003), or the Salt Range in the Himalayan foreland of Pakistan (Baker et al., 1988), amongst others. Salt in fold-and-thrust belts can occur as squeezed diapirs (e.g., Callot et al., 2012), along thrust welds (e.g., Hossack, 1995; Vidal-Royo et al., 2021), and at the base of the thrust sheets (e.g., Davis & Engelder, 1985; Hudec & Jackson, 2006) (Figure 1b). But in general, contractional structures in salt-influenced fold-and-thrust belts tend to show limited amounts of salt. Lack of extensive salt exposures may lead to question the original salt budget, and consequently the role of salt tectonics in shaping stratigraphic and structural development. Only under certain conditions, such as very arid climates, salt can be preserved as allochthonous salt sheets (e.g., Hudec & Jackson, 2006).

We aim to characterize the structure of fold-and-thrust belts which involve late syn-rift to post-rift minibasins and related salt structures, and to obtain a series of diagnostic features and templates that allow for their identification and understanding and develop predictive templates in salt-influenced contractional systems. Our purpose is to go a step further into the comprehension of the influence of the inheritance and surface processes during mountain building and discuss salt mobilization from thick post-rift salt basins to the apparent absence of salt in fold-and-thrust belts. To accomplish these goals, we use a set of sandbox analog models to illustrate three different scenarios of the evolution of inverted salt-bearing rifted margins. Experimental results are presented, discussed, and compared to the Northern Calcareous Alps of Austria.

2. Analog Modeling

2.1. Rationale

The aim of this work is to provide geometric and kinematic templates for fold-and-thrust belts involving salt-bearing rifted systems. Our purpose is to unravel diagnostic features (i.e., geometries) linked to natural processes operating upon the formation of salt-bearing rifted margins, as in modern-day passive margins of Angola (Ge et al., 2020), Brazil (Espírito Santo and Campos basins, Blaich et al., 2011; Pichel et al., 2021), the Gulf of Mexico (e.g., Rowan, 2020a, 2020b) or South Gabon (Moore & Blanchard, 2017), and its subsequent incorporation into orogenic systems, as it is the case of the Northern Calcareous Alps (Granado et al., 2019; Strauss et al., 2020), the Southern Pyrenees (López-Mir et al., 2014a, 2014b) or the Central High Atlas (e.g., Saura et al., 2014; Calvín et al., 2018). This work represents the continuation of the experimental program presented in Granado et al. (2022). In their work, these authors present a series of physical analog models aiming to analyze the influence of differential loading versus dominant gliding (*sensu* Brun & Fort, 2011) on salt-bearing passive margins and their characteristic tectonostratigraphic architecture. In this present work, we have followed up the experimental program of Granado et al. (2022) by studying the geometries resulting from the contractional deformation of the rifted margin models with and without surface processes (i.e., erosion and sedimentation).

Table 1
Material Properties and Dynamic Scaling Parameters of the Experimental Program

Parameter	Equation	Model	Nature	Scaling ratio
Length		1 cm	0.5 km	2×10^{-5}
Density				
Sand/Brittle Rocks		1,500 kg/m^3	2,567 kg/m^3	0.58
Model salt/Décollements		972 kg/m^3	2,200 kg/m^3	0.4
Gravity		9.8 m/s^2	9.8 m/s^2	1
Cohesion		55 Pa	50×10^6 Pa	1.1×10^{-5}
Deviatoric stress	$\sigma = \rho \cdot g \cdot L$	121 Pa	1.17×10^7 Pa	1.0×10^{-5}
Ductile layer viscosity		1.6×10^4 Pa·s	10^{18} Pa·s	1.6×10^{-14}
Strain rate	$\varepsilon = \sigma/\eta$			6.5×10^8
Time	$t = 1/\varepsilon$	1 hr	74,000 years	1.5×10^{-9}
Velocity	$V = L{\cdot}\varepsilon$	0.5 cm/hr	3.4 mm/y	1.3×10^4

Note. Scaling ratio refers to the model to nature relation of a given magnitude or parameter. Units are given in IS standards.

2.2. Experimental Methodology

2.2.1. Analog Materials and Scaling

Models were performed using appropriate modeling materials to simulate upper crustal deformation (see Adam et al., 2005; Davy & Cobbold, 1991; Dell'Ertole & Schellart, 2013; Lohrmann et al., 2003; Schellart & Strak, 2016; Schellart, 2000; Weijermars & Schmeling, 1986) according to scaling principles (Table 1). Rhodosil GUM FB from Bluestar Silicones, a transparent high-viscosity polydimethylsiloxane silicone polymer, was used to simulate natural rock salt. This polymer behaves as a nearly-Newtonian fluid having very low yield strength and a stress exponent n of ~1 at experimental strain rates. The density of the polymer at room temperature is 972 kg/m^3 while its viscosity is 1.6×10^{-4} Pa·s when deformed at an experimental strain rate of 1.83×10^{-4} cm/s (Dell'Ertole & Schellart, 2013). Hereinafter, the term *model salt* will be used instead of silicone polymer, and the standard salt tectonics nomenclature to describe polymer-related structures. On the other hand, dry well-sorted quartz sand (i.e., 98% pure silica) with an average grain size of 199 μm, a mean coefficient of friction (φ) of 0.6, and an average angle of internal friction (ϕ) of 34°, a bulk density of 1,500 kg/m^3 and cohesive strength of ~55 Pa (Ferrer et al., 2017) was used to simulate upper crust brittle rocks. Sand is characterized by an elastic/frictional plastic behavior with transient strain hardening prior to transition to stable sliding (e.g., Adam et al., 2005; Lohrmann et al., 2003), being a reasonably good mechanical analog for such rocks.

Analog models were carried out following geometric and dynamic scaling principles. Geometric scaling guarantees that corresponding ratios of dimensions and angles are comparable between analog models and nature. The geometric scaling ratio is determined by the procedure for dynamic scaling, which in analog modeling studies has been established for quite a long time (e.g., Davy & Cobbold, 1991; Koyi et al., 1993; Vendeville et al., 1995; Warsitzika et al., 2015, 2021; Weijermars & Schmeling, 1986). This means that 1 cm in our analog models represents 0.5 km in nature. Dynamic scaling requires trajectories and ratios of acting forces to be equal and that rheological behaviors of the involved materials are similar (e.g., Weijermars & Schmeling, 1986).

Table 2
Summary of the Experimental Program

Model	Passive margin stage	Shortening	Surface processes
Model 1	DB + GD + GD	–	–
Model 2	DB + GD + GD	50 cm	–
Model 3	DB + GD + GD	50 cm	Erosion and sedimentation

Note. The table includes rifted margin stage doming processes for each sequence, the amount of shortening and the implemented surfaces processes. Note that downbuilding (DB) was a continuous process that coexisted with dominant gliding (DG).

2.2.2. Experimental Program, Set up and Procedure

Our experimental program includes three models that represent different scenarios of the development and incorporation of a salt-bearing rifted margin into a fold-and-thrust belt (Table 2). Model 1 involves only the rifted margin stage. Model 2, involves the rifted margin stage, followed by shortening and Model 3 involves the rifted margin stage followed by shortening with erosion/sedimentation. Common to all the models, the modeling program set up aims to represent the final stages of a rifted margin, once thermal subsidence leads to the progressive seawards tilting of the margin hosting

a late syn-rift to early post-rift salt basin type (Rowan, 2014). The pre-salt rifted margin structure in the model was preproduced according to a stretched and thinned margin in the inception of necking and break up. In this situation and as an experimental simplification, the salt-sediment system evolution contemplates a first stage of pure differential loading followed by a stage of dominant gliding. Alternative scenarios with different amount of differential loading versus dominant gliding are presented and discussed in Granado et al. (2022). The potential effects associated with a prograding sedimentary slope are here not considered, partly because we aim to model carbonate growth on top of salt. In terms of rifted margin architecture, our models simulate the transition from a proximal to a distal domain across a necking to hyperextended area including the shelf, the shelf-break and the slope settings (Granado et al., 2022; Péron-Pinvidic et al., 2019).

During the subsequent contraction stage, the amount of shortening was set to ensure the whole rifted margin was inverted and incorporated into the orogenic wedge. Syn-contractional surface processes were only applied to Model 3 and involved erosion of the orogenic hinterland while the eroded material was deposited in the foreland basin and in piggy-back basins. In addition, in Model 3, extruded model salt was completely removed from the surface. For the model with no erosion or sedimentation (i.e., Model 2), extruded salt was left to flow over growing anticline structures and down into piggy-back basins.

An experimental rig with maximum dimensions of 170 cm long, 30 cm wide and 30 cm high was used. Experimental materials were laterally bounded by two glass side walls, and a mobile wall (i.e., the backstop) resting on a basal metal table. Lying over the basal metal plate, the experimental setup (Figures 2a and 2b) included a basinward-dipping basement step in the proximal area, a basement wedge in the distal area; an outer high was also included, representing a pre-salt basement topography (e.g., Bronner et al., 2011; Peron-Pinvidic & Manatschal, 2010; Uranga et al., 2022). All these elements were set on a basal plate tilted 2.3° basinwards (Figure 2b). On top of such configuration, a 93 cm long by 30 cm wide (46.5 km long by 15 km wide in nature), tapered model salt basin was laid from a landward-located pinch-out to the outer high. The model salt basin was 3 mm thick above the basement step and beyond this point it thickened basinwards from 3 to 23 mm thick (150 m–1,150 km thick salt unit in nature). Overlying the model salt basin, a blue sand layer extends from beyond the model salt pinch-out to the outer high to represent a pre-kinematic layer (termed as PK in the stratigraphic pile of Figure 2a). The syn-kinematic sequences are made of a series of red, white, brown and white sand layers; sequence boundaries were made by adding a grain-size-thick black sand marker layer (Figure 2a). The syn-kinematic sequences are labeled as Downbuilding sequence 1 (DSq1), deposited under pure differential loading boundary conditions, and Gliding sequences 1 and 2 (GSq1 and GSq2), deposited under dominant gliding boundary conditions, respectively. Regional sedimentation level increased 1 mm at each sedimentation event. The syn-kinematic sequences are covered by a post-kinematic sequence (PG, Figure 2a) made of a triplet of green, white and green sand layers. Each of these layers was poured and leveled after tilting the experimental rig 0.15° basinwards, resulting in tapered sequences whose thickness varies from 1 mm above the model salt pinch-out to 3 mm on the shelf-break (Figure 2c). Such tilting simulates thermal subsidence. Beyond the shelf-break, sand was sprinkled to fill low-lying areas and represents distal margin condensed sequences. Sedimentary rate and regional subsidence promoted salt evacuation and salt wall growth while preventing massive model salt extrusion (Granado et al., 2022).

The architecture of the modeled rifted margin includes a proximal basin, broadly undeformed and floored by thin model salt, a salt wall-minibasin province, and a distal raft system. Minibasins (i.e., Mb 1, 2; Figures 2a and 2c) and salt walls (SW1, 2 and 3, respectively; Figures 2a and 2c) were modeled as largely bidimensional features extending along the whole width of the experimental sandbox and their widths progressively increasing seawards (Figures 2a–2c), much like those reported for natural systems such in Angola or Gabon (e.g., Eichenseer et al., 1999; Ge et al., 2020; Moore & Blanchard, 2017).

Onset of salt evacuation was triggered by pouring the first syn-kinematic sand layer around the location of *what-would-be* the minibasin depocenters (minibasin seeding areas in Figure 2b). Sand deposited in such a way led to a localized sedimentary differential loading that triggered minibasins vertical sinking, while model salt is evacuated from below the minibasin depocenters toward flanking salt walls (e.g., Ferrer et al., 2022; Rowan & Vendeville, 2006; Santolaria, Ferrer, et al., 2021; Santolaria, Granado, et al., 2021; Warsitzka et al., 2013). Additional sand layers filled the accommodation space created by the minibasin's sinking which, in its turn, created positive feedback between sedimentary differential loading and sinking. Downbuilding sequence 1 (DSq1) was deposited under such conditions.

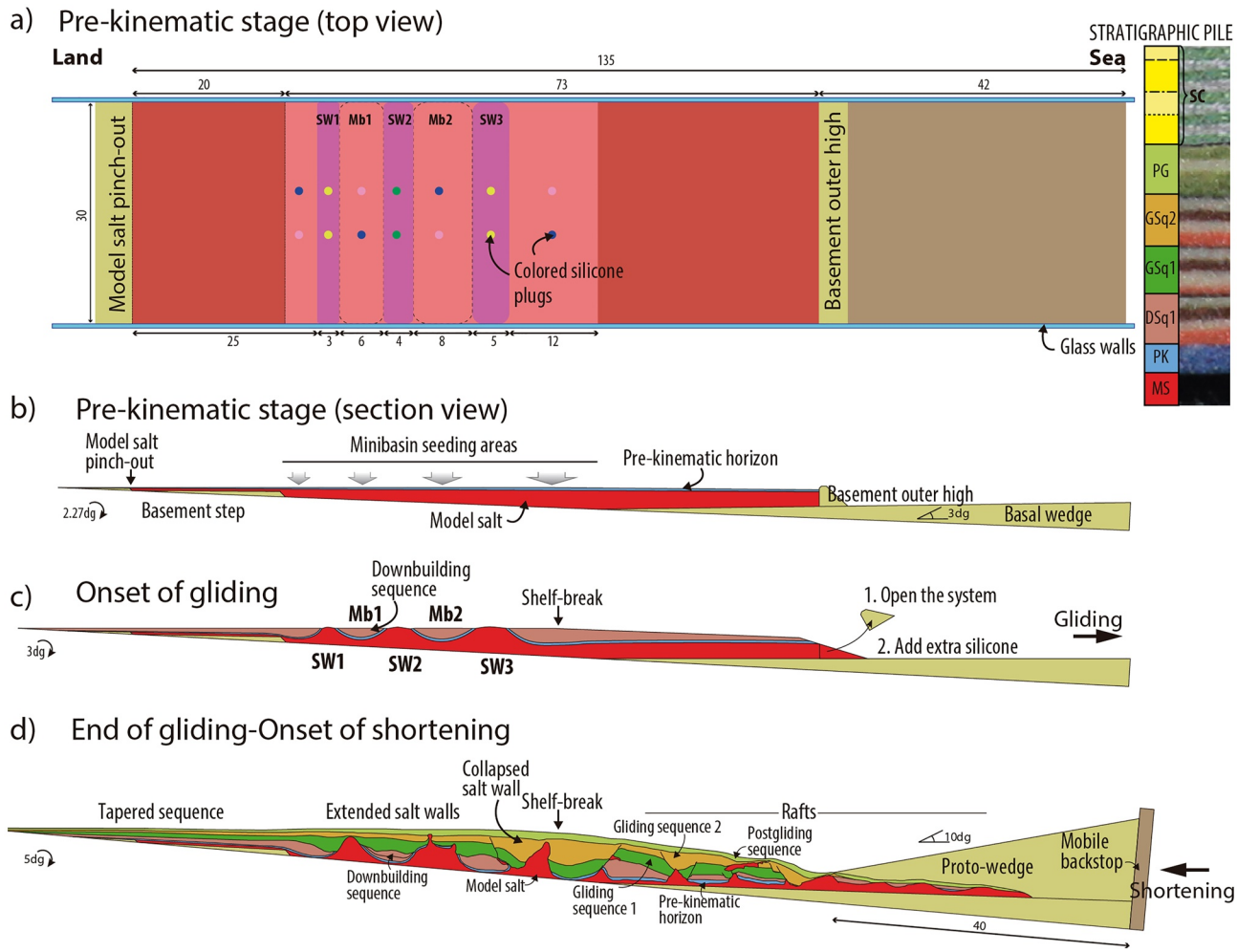

Figure 2. Experimental setup. (a) Left, top view of the model setup showing location and dimensions of key elements: model salt pinch-out, minibasins (light pink), salt walls (dark pink) and basement outer high (yellow); right, stratigraphic log representing the model salt, the pre-kinematic layer (PK), the downbuilding sequence (DSq), the gliding sequences (GSq1 and GSq2), the post-gliding sequence (PG) and the syn-contractional package (SC). b to d, section views showing the main elements of models' setup at pre-kinematic stage (b), at the transition from downbuilding to gliding (c); and featuring a simplified rifted margin model soon before shortening starts.

Then, gliding of the experimental sand pack was achieved by removing the sand-built outer high and thus opening a free toe for the salt-sediment system (Figure 2c). Upon toe opening, model salt was no longer confined, allowing the salt-sediment system to move seawards. Gliding sequences 1 and 2 (GSq1 and GSq2) were deposited under such conditions. Tilting of the experimental rig upon the sedimentation of each of these sequences reinforced gliding by increasing the inclination of the basal table, simulating thermal subsidence. Note that despite gliding being dominant during this stage, differential loading by sedimentation continued, as aided by the deposition of each new sand layer. Regardless contractional structures have not developed in the distal domain, as characteristic of linked gravity gliding systems detached on salt, they are represented in the model by the thrust at the front of the allochthonous salt sheet and gradients on displacement vectors in the distal domain (Figure 3). The displacement of the allochthonous model salt would represent the allochthonous salt sheets moving above oceanic crust in the distal domains of many passive margins, such as Golf of Mexico and Atlantic margins (Hudec & Jackson, 2006; Rowan, 2017). Moreover, our models have focused on the contractional reactivation of the salt and extensional structures of the proximal and necking domains.

At the end of the rifted margin stage, the entire experiment was covered by a grain-size thick black layer marker on top of which an orthogonal pattern was drawn using glass microbeads. Before the onset of shortening, a proto-wedge was built on the deepest part of the rifted margin slope aiming to rapidly reach the critical taper of

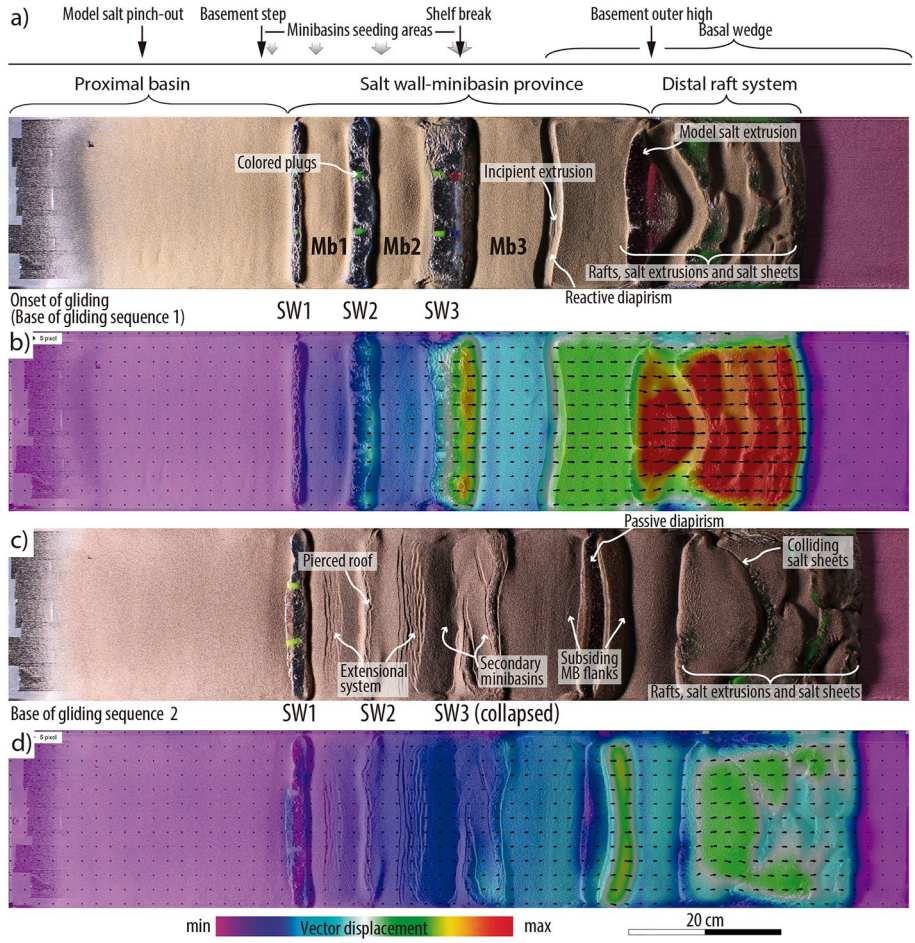

Figure 3. Representative top views and related displacement vector field color maps of Model 1 soon after the onset of gliding (a, b), and later on, during gliding sequence 2 (c, d). Main structural elements of the analog model set up are displayed at the top.

the orogenic wedge (e.g., Granado et al., 2017; Malavieille & Konstantinovskaya, 2010; Konstantinovskaya & Malavieille, 2011; see Figure 2d). The proto-wedge original dimensions were 40 cm long by 11 cm high, with a landward slope of 10°. In nature, such a wedge represents an older imbricate system coming from a more distal part of the rift basin and thrusting over the raft system (Tavani et al., 2021). Shortening was achieved by a computer-controlled motor-driven worm-screw that pushed the mobile backstop forwards (push-from-behind or indentation experimental design, Peltzer et al., 1982; Tapponnier et al., 1982) at a fixed velocity of 5 mm/hr. Total shortening was 50 cm for Models 2 and 3.

Surface processes in Model 3 included syn-shortening erosion and sedimentation. Up to nine events of erosion and sedimentation were performed; the first one of these was carried out after 10 cm of shortening, and then each approximately 5 cm of shortening. The erosion regional levels were established from the orogenic taper evolution observed in Model 2 and varied from 1° (first to third syn-shortening layers), 1.5° (fourth and fifth syn-shortening layers) to 2° (sixth to ninth syn-shortening layers). This represents a positive correlation between the increase of topography and the regional level of erosion, common during mountain building in natural orogens (e.g., Curry et al., 2021). Each regional level of erosion was drawn on the glass-wall of the deformation rig. Erosion profiles intersect the modeling sand pack 5 cm beyond the model salt pinch-out and extend up to the backstop. Once drawn, all the material above the erosion profile was manually removed using a vacuum cleaner. Extruding model salt was systematically removed along the whole extension of the experiment. The amount of removed material was then calculated. One third of the eroded material is then sedimented below the erosion regional level as a new sand layer (white and green sand layers, Figure 2a). Such balance between eroded and sedimented material

has been chosen as a fitting approximation to what has been reported for fold-and-thrust belts developed at the pro-wedge in natural orogenic systems (e.g., Beamud et al., 2011; Morris et al., 1998; Rushlow et al., 2013; Sinclair et al., 2005; Willet, 1999), where the sediment routing system is largely parallel to the strike of the active belt (e.g., Costa et al., 2010; Garcés et al., 2020; Muñoz et al., 2013; Schlunegger & Castelltort, 2016). At each erosion-sedimentation event, syn-shortening sedimentation was controlled by the morphotectonic evolution of Model 3: first layers were deposited on low relief areas at the toe of the advancing front and then, as those lows were overfilled, syn-shortening sedimentation advanced toward the foreland, leading to a regionally prograding but locally aggradational system.

As for modeling limitations, no thermal effects or lithospheric flexure were simulated; modeling materials laid over a rigid table which represents a rigid and flat basement. The onset of gliding was triggered by removing the sand-built outer high which simulates the destabilization of the initially confined salt basin after crustal hyper-extension and the slope developed upon necking and thermal subsidence (Granado et al., 2022). Then, salt overcomes the outer high and glides basinwards as an allochthonous salt sheet as in the Gulf of Mexico (e.g., Hudec et al., 2013), the South Atlantic (e.g., Aslanian et al., 2009) or the North Atlantic (e.g., Adam & Krezsek, 2012). In nature, such process may lead to a progressive incremental gliding of the margin rather than a sudden response of the margin after the removal of the high as reproduced in our models. The addition of the proto-wedge before shortening represents an instantaneous emplacement of a thrust system on top of the distal raft system. However, in nature, the gradual emplacement of imbricates may have a slightly different effect on the salt evacuation from the distal raft system ahead of the thrust wedge.

2.2.3. Data Capture and Analytical Techniques

The morphometric evolution during the different phases of the experiments was recorded by time-lapse high-resolution digital photographs. Top and latera photographs were taken at 90 s intervals and were then used to generate videos for kinematic analysis.

Particle image velocimetry (PIV) was also used as a complementary tool for kinematic analysis. PIV can provide a basis for discrete differential and total displacement and strain analysis by tracking movement, at the grain scale, in the model sand surface (Adam et al., 2005; Raffel et al., 2013; Tischer et al., 2001). PIV was carried out using DaVis 8.2.0 software from time-lapse photography. PIV technology can document grain-scale movements at a very high temporal and spatial resolution and can provide movement vectors for all points in a deforming sand-wedge without relying on predefined markers.

At the end of each experiment, the entire model was preserved to be longitudinally sectioned at 3 mm spacing; every section was captured by means of high-resolution digital photography cameras. A 5 cm wide section along each side of the experiments was discarded to remove any possible border effects. Photographed sections were used to interpret the structural and stratigraphic architecture of the models and to generate voxels in image-processing software to further constrain the 3D geometries of the model which allow the creation of virtual slices of the sandbox (Dooley et al., 2009; Ferrer et al., 2016; Granado et al., 2017; Santolaria, Ferrer, et al., 2021; Santolaria, Granado, et al., 2021). Section restorations (Roma, Vidal-Royo, et al., 2018; Santolaria, Ferrer, et al., 2021; Santolaria, Granado, et al., 2021) have been used to reconstruct the pre-shortening configuration inherited from the rifted margin stage (Models 2 and 3) and also the evolution during contraction of Model 3.

3. Results

3.1. Rifted Margin Stage

In this section, Model 2 illustrates the top view morphology and kinematic evolution during the rifted margin stage (Figure 3) and Model 1, the only one preserved after this stage, exemplifies the overall architecture of the rifted margin (Figure 4) as well as close-up details of resulting geometries of minibasins and salt walls in cross-section (Figure 5).

During the downbuilding stage, model salt was confined, and differential loading led to minibasin sinking and salt evacuation from below minibasins' depocenters to their flanking salt walls. On top of salt walls, the uprising model salt initially arched the pre-kinematic sequence until eventually piercing it, soon before the onset of gliding. Then, upon the toe opening (onset of gliding), the salt-sediment system glided downwards resulting in salt-detached extension which rapidly propagated landward (i.e., upslope) from the toe to the salt wall-minibasin

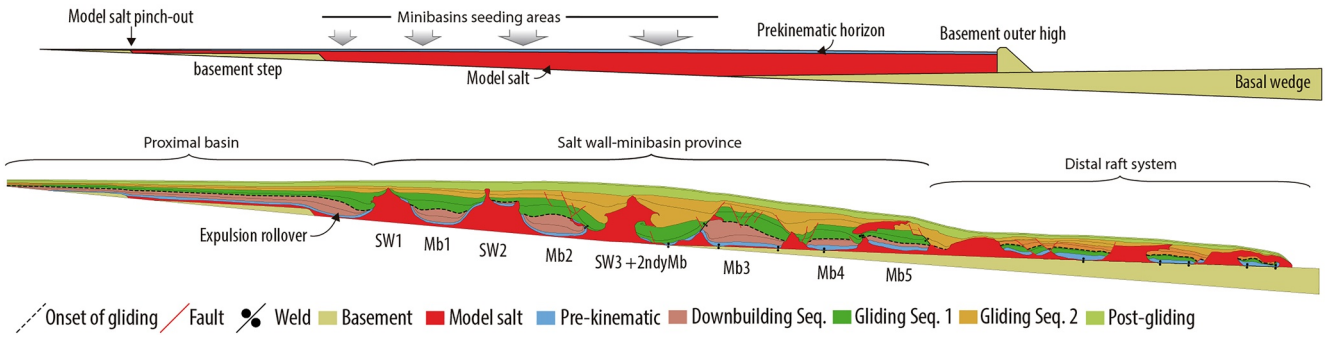

Figure 4. Shape of the original salt basin for reference (top) and representative cross section of Model 1 (bottom) at the end of the rifted margin stage. Modified from Granado et al. (2022).

provinces but did not reach the proximal basin (Figure 3a). Extension triggered reactive to passive diapirism (Figure 3a), model salt extrusion along the slope, and the widening of salt walls (i.e., cryptic extension, Vendeville & Jackson, 1992) (Figure 3a). The red to very dark blue color gradation in the PIV color map of Figure 3b reveals that in between salt walls distal rafts translate more (and faster) than proximal minibasins. Besides, plain colors point out that minibasins and rafts are passively transported downslope and therefore, new and previous salt walls, as the weakest discontinuities of the salt-sediment system, accommodate most of the extension and compartmentalize the modeling package. PIV measurements also show that distal salt walls accommodate more extension than proximal ones. Downbuilding by differential loading was still ongoing, especially in SW1 and Mb1, where extension was minimum, so that model salt kept on extruding.

As the models evolved, gliding slowed down, as illustrated by the top view and equivalent PIV color map of the base of GSq2 (Figures 3c and 3d, respectively). In the distal raft system, extruded model salt formed salt sheets that eventually coalesced and formed salt canopies. In the salt wall-minibasin province, SW3 collapsed forming secondary minibasins (Figure 3c) and promoting further model salt evacuation from the salt wall. The flanks of primary welded minibasins (sensu Jackson & Cramez, 1989) also started to subside resulting in the formation of incipient turtle anticlines and additional model salt migration toward salt walls. Turtle formation is evidenced by the extensional faults developed along the axis of the minibasins observed in the top views (Figure 3c). PIV measurements illustrate the slowdown of gliding through time; the color map on Figure 3d displays low to medium displacement vector colors which still displays a landward decreasing trend. Extension is no longer as compartmentalized as before and still does not reach the proximal basin.

Section of Model 1 displays a seaward thickening proximal basin that terminates in an expulsion rollover (sensu Ge et al., 1997), flanked by SW1 and situated beyond the basement step (Figure 4). The salt wall-minibasin province involves up to five minibasins flanked by salt walls associated with diapir shoulders and wings and a large secondary minibasin developed during the collapse of SW3. Most of these primary and secondary minibasins are primary welded. The distal raft system consists of raft blocks flanked by wide model salt bodies. Some of these rafts show incipient extension and some others are capped by extruded model salt (Figure 4).

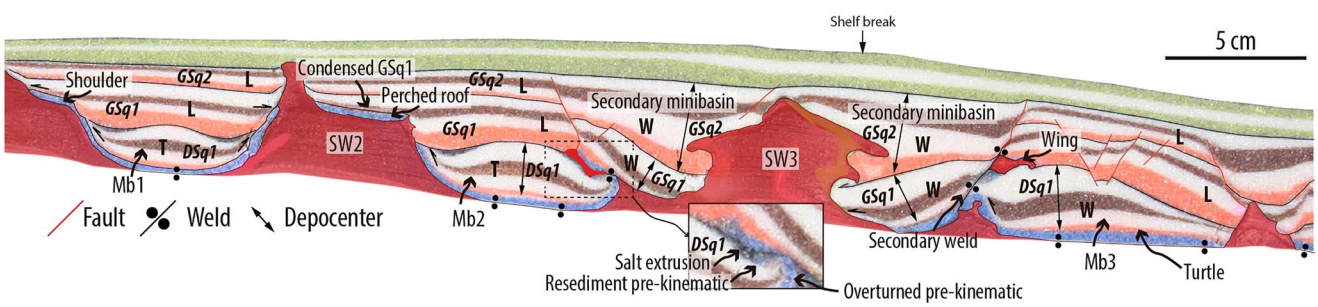

Figure 5. Close up and interpretation of minibasin 2 and 3 and related structures (i.e., collapsed salt walls and secondary minibasins) of Model 1. Modified from Granado et al. (2022).

A close-up view of the salt wall-minibasin province displays perched roofs, turtle structures, collapse salt walls, primary, secondary and tertiary welds, cusps, wings, salt walls and salt sheets (Figure 5). In those minibasins initially flanked by salt walls (Mb1 and Mb2) the internal geometry of the downbuilding sequence is that of troughs (Rowan & Weimer, 1998), with younger syn-kinematic layers onlapping against the pre-kinematic layer (see Mb 1 and 2, Figure 5). Overlying the downbuilding sequence, gliding sequences (GSq1 and 2) conform to layer geometries (sensu Rowan & Weimer, 1998), eventually deposited coevally with extension of minibasins and the formation of turtle structures (Mb3, Figure 5). Such tectonostratigraphic architecture reflects the switch from a salt-sediment system growth under differential loading to dominant gliding. The time of model salt piercing and subsequent extrusion is marked by the occurrence of resedimented sand (i.e., blue sand) along the peripheral synclines and on top of the youngest layer of the downbuilding sequence and the presence of extruded model salt on top of these youngest sequences (Figure 5, close up detail). Model salt extrusion is locally related with the deformation and overturning of the pre-kinematic and DSq1 layers (Figure 5). Younger layers of the gliding sequence 1 (GSq1) onlap onto the pre-kinematic layer (Mb1, Figure 5), are eventually unconformable on the tip of it (landward flank of Mb2) or laid on top of salt wings (Mb2 and 3). Older layers of the gliding sequence 1 prograde landwards and rest onto the pre-kinematic layer. Sand layer progradation constituted large diapir shoulders (Mb1) or perched roofs (Mb2) (Figure 5).

One of the most outstanding features is the secondary minibasin formed upon the collapse of SW3. There, GSq1 rests on the pre-kinematic layer or directly on top of the model salt. First and second gliding sequences display wedge geometries thickening toward the remaining SW3. Former wings were shut off by the sinking of secondary minibasins, creating secondary welds (Figure 5). In between minibasins, model salt bodies display a variety of geometries from wide salt walls topped by condensed sequences or perched roofs (Mb1 and 2) to upward-narrowing geometries with evidence of model salt extrusion (Mb3) or triangular-shaped diapirs (Figure 5).

3.2. Shortening of Salt-Bearing Rifted Margins

Model 2 involved the contraction of the salt-detached rifted margin without the influence of syn-contractional surfaces processes. Shortly before the onset of contraction, some inherited structural features remained active, such as the extensional collapses in SW2 and SW3 (Figure 6a), which indicated that salt-detached extension was still ongoing. At the onset of contraction, model salt evacuated from beneath the proto-wedge, flowed toward its tip, and eventually extruded to the actively deforming surface (Figure 6a). During the first 21 cm of shortening, most of the contractional deformation focused on the advancing proto-wedge and on the reactivation of the collapsed SW3. Shortening of the proto-wedge and the distal raft system below led to a massive extrusion of model salt from different points along the proto-wedge toe (Figure 6b). At that point, deformation reached SW1 and SW2, as indicated by the rejuvenation of a salt stock associated to SW1 and the arching of the roof of SW2 (Figure 6b). Further shortening led to the reactivation of SW2 by backthrusting and SW1 by additional diapiric rise and roof arching (Figure 6c). Model salt extrusion from the proto-wedge toe continued and the resulting salt sheet advanced over the relief created after reactivation of the collapsed SW3. Synchronous thrusting was also registered in the proto-wedge (Figure 6c). After 43 cm of shortening (Figure 6d), model salt fountains at the toe of the proto-wedge were still active. Nevertheless, most of the shortening was accommodated by closure of SW2, as evidenced by roof arching and associated outer-arc extension. In the case of SW1, the squeezed model salt pierced its roof and extruded. Deformation reached the foreland where a box-fold nucleated at the model salt pinch-out. Between this stage and the end of the experiment (Figure 6e), this box-fold grew synchronously with further deformation of SW1 and SW2 and limited proto-wedge model salt extrusion.

Restored section of Model 2 (Figure 7a) displays the same major features of Model 1: a proximal basin, a salt wall-minibasin province and the distal raft system. The proximal basin is also characterized by a seaward thickening geometry that culminates in an expulsion rollover related to the basement step. At the transition to the salt wall-minibasin province, this expulsion rollover is flanked by SW1, a mushroom-like diapir capped by gliding sequence 2. Mb1 is slightly asymmetric, expands seawards and is flanked by a relatively wide SW2. Mb2 exhibits a turtle geometry and its related extensional system. GSq1 and GSq2 display significant stratigraphic expansion and thickening associated with the formation of a secondary minibasin formed due to the extensional collapse of SW3. After the collapse of SW3, it split into two model salt accumulations separated by a flaring upwards feature made of gliding sequences 1 and 2 (Figure 7). Mb3 also shows a turtle geometry with a lateral expansion of GSq2 toward SW3. The distal raft system consists of one major and two smaller rafts where the entire stratigraphic

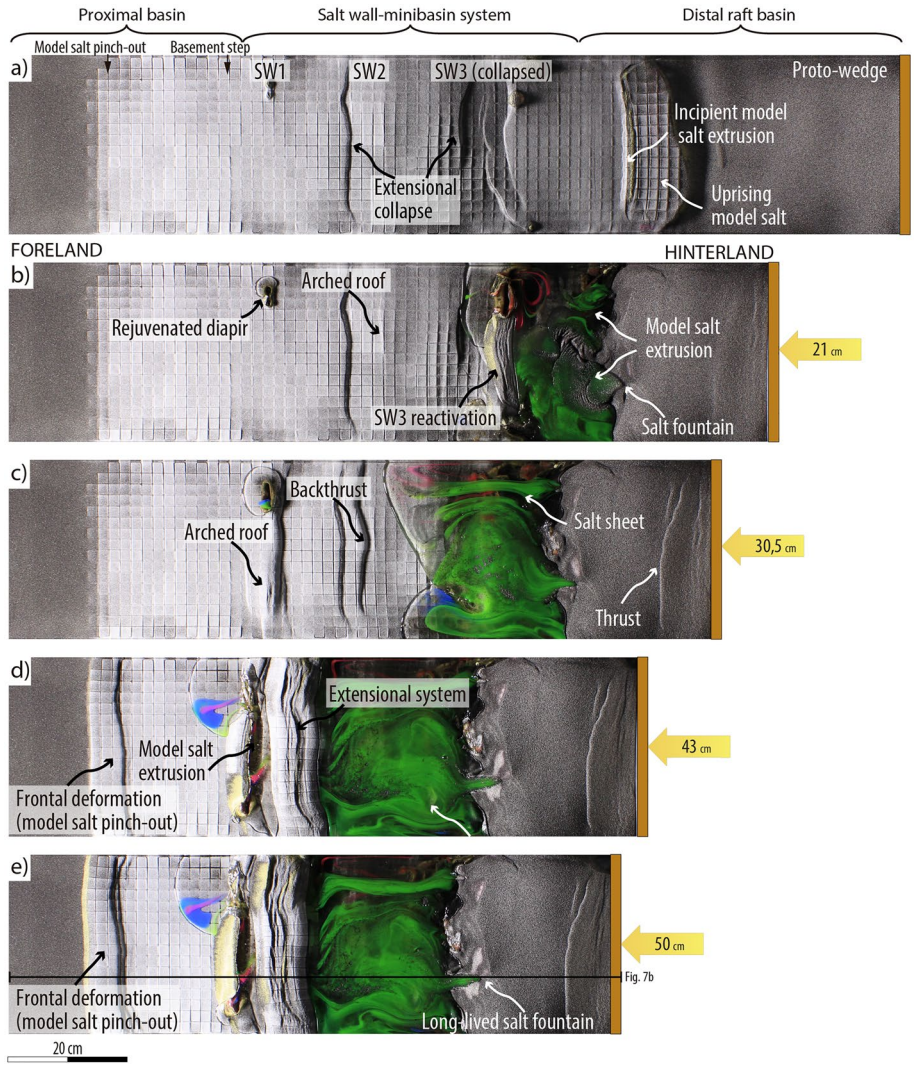

Figure 6. Top view evolution of Model 2.

succession is present. The three rafts are mostly covered by salt sheets, which in turn host secondary minibasins, minor diapirs and short-wavelength extensional faults occur.

Once shortened, the aforementioned features were incorporated in the orogenic sand wedge (Figure 7b). In the hinterland, the basal wedge displays a 29° tapered imbricate system of foreland-directed thrusts (Figure 8a). The proto-wedge above was slightly folded and thrusted. In between these elements, the distal basin features a complex folded imbricate system of secondary minibasins, proto-wedge toe sand and derived debris and patches of model salt (Figures 8b and 9a). Secondary minibasins occurred as normal, steeply dipping to completely overturned panels, limited by secondary welds and thrust faults, some of which are facing downwards (Figure 8a). The raft system was partially imbricated together with the basal wedge. The contact between them features a set of welds and model salt remnants (Figure 8a). Mb3 and Mb2 were transported landwards and show no evidence of internal deformation or tilting, their original geometry and location of primary welds seem to have been preserved (Figures 7b and 8a, b). Conversely, in between both, SW3 was squeezed and its roof uplifted. A secondary minibasin became fully encased within SW3 and behaved as a rigid block that prevented further diapir squeezing (Figure 9b), a similar process to that described in Duffy et al. (2017). Mb2 displays two different extensional systems, a central system related to the evolution from a trough-like to a turtle minibasin and a second system associated with the collapse of SW3. SW2 narrowed to approximately one fourth of its original shape and its roof arched until it finally thrusted seawards (Figures 7b and 8a).

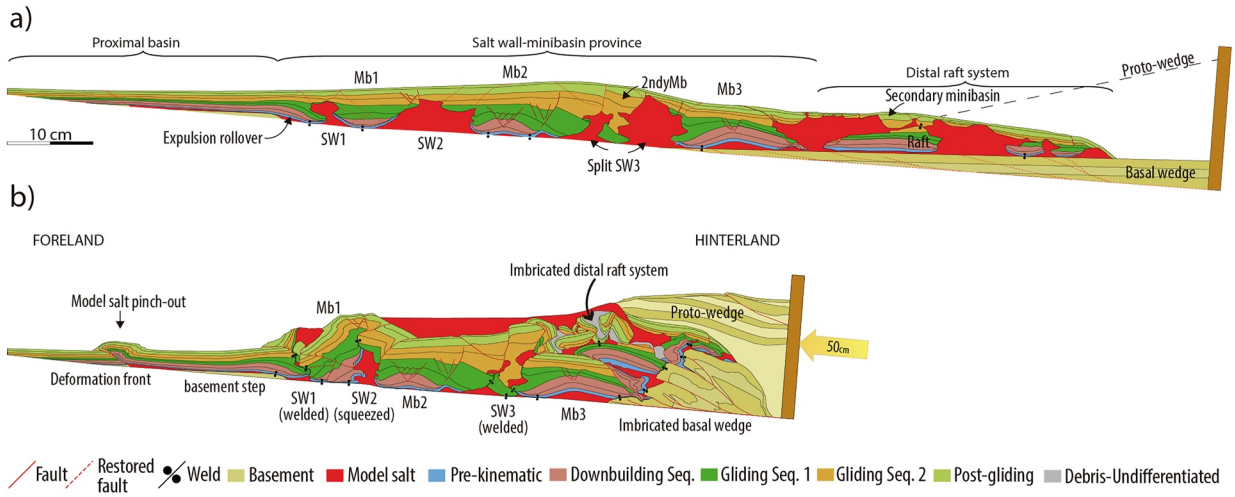

Figure 7. Restored version at the end of the rifted margin stage (a) of a representative section (b) of Model 2. See Figure 6 for location.

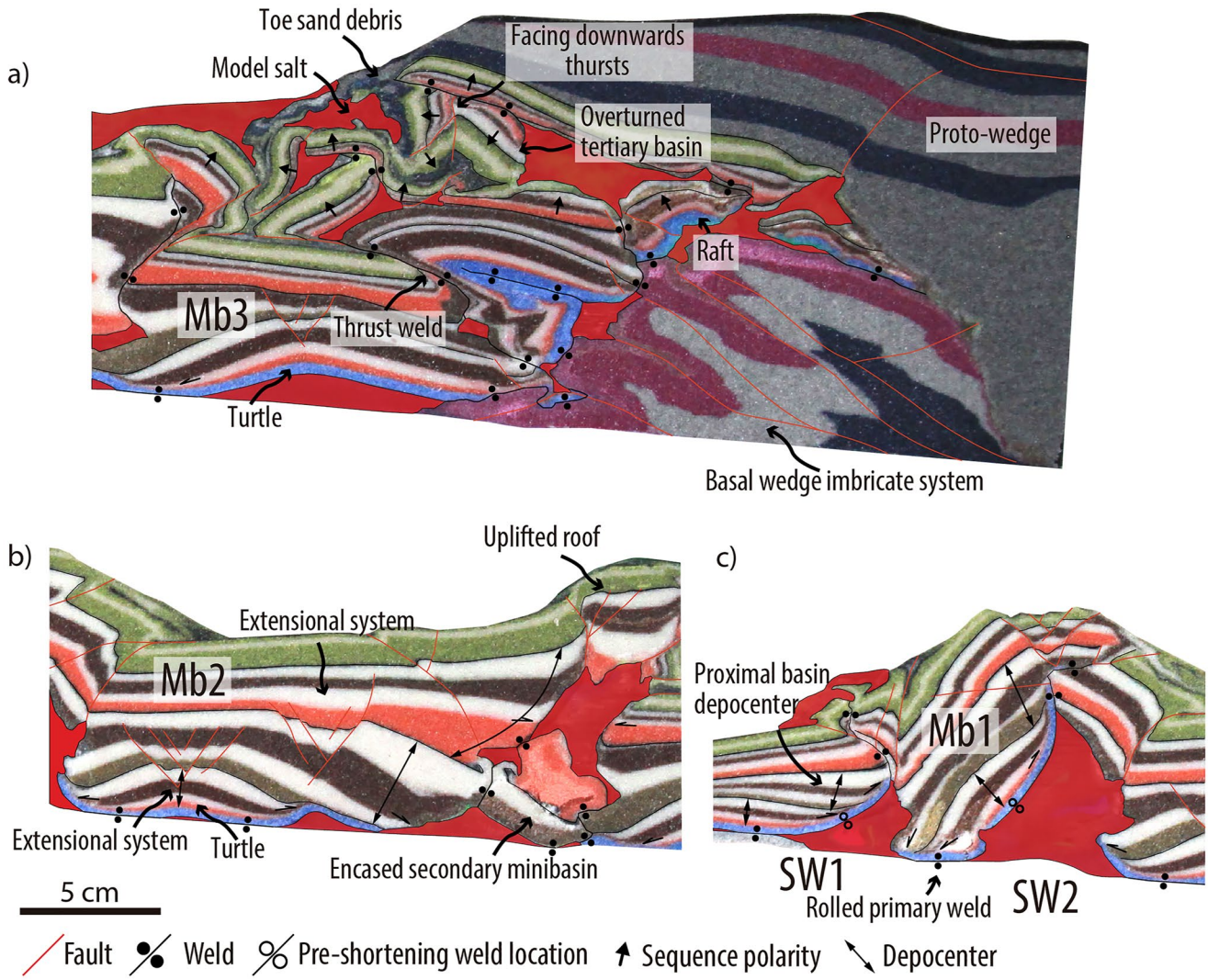

Figure 8. Representative close ups of Model 2 showing (a) minibasin 3 and the basal wedge imbricate system, the deformed distal raft system and the proto-wedge, (b) minibasin 2 and salt wall 3 and (c) the landward counter-clockwise rotation of minibasins 1 between salt walls 1 and 2.

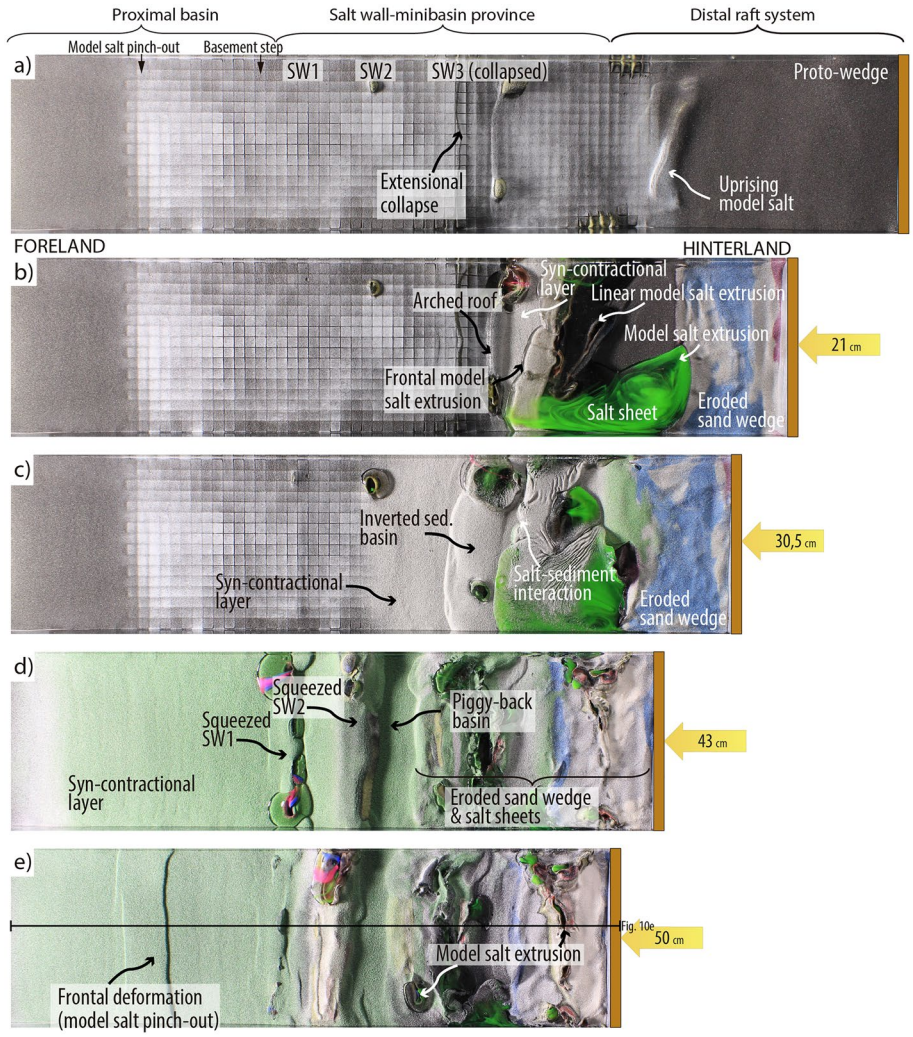

Figure 9. Evolution of Model 3 illustrated by top views at (a) the onset of shortening, (b) immediately before deposition of syn-contractional layer 3 (21 cm of shortening), (c) layer 5 (30.5 cm of shortening) and (c) layer 8 (43 cm of shortening) and (d) at the end of shortening (50 cm of shortening).

One of the most prominent features of the sections is the forelandward tilted Mb1. Mb1 attained as much as 50° of counterclockwise rotation around a sub-horizontal axis (Figures 7b and 8c). Tilting was accompanied by the migration of the original position of its primary weld which is now situated in the landward flank of the minibasin (i.e., a *rolled primary weld*, sensu Santolaria, Ferrer, et al., 2021; Santolaria, Granado, et al., 2021). SW1 depicts a nearly vertical sigmoidal secondary weld rooted on a model salt accumulation. Such model salt accumulation substituted what it was once the primary weld of the expulsion rollover (Figures 7b and 8c).

3.3. Shortening of Salt-Detached Rifted Margins With Surface Processes

Model 3 illustrates the role played by surface processes during shortening. Before contraction and like in Model 2, the extensional collapse of SW3 was still active. As observed in Model 2, in this model, the model salt also evacuated from beneath the proto-wedge and accumulated at its tip (Figure 9a). During the first 21 cm of shortening, there was salt extrusion along the proto-wedge: at its tip, as a frontal extrusion, at its toe, as a slight oblique linear salt extrusion, and in its center (see green salt sheet in Figure 9b). Up to that point, the low area between the toe of the advancing proto-wedge and the shelf break acted as an underfilled basin, hosting all syn-contractional sediments. Then, salt sheets advanced and covered the syn-contractional sediments (Figure 9b). From 21 to 30.5 cm of shortening, continuous erosion and shortening of the orogenic wedge kept the model salt extrusions

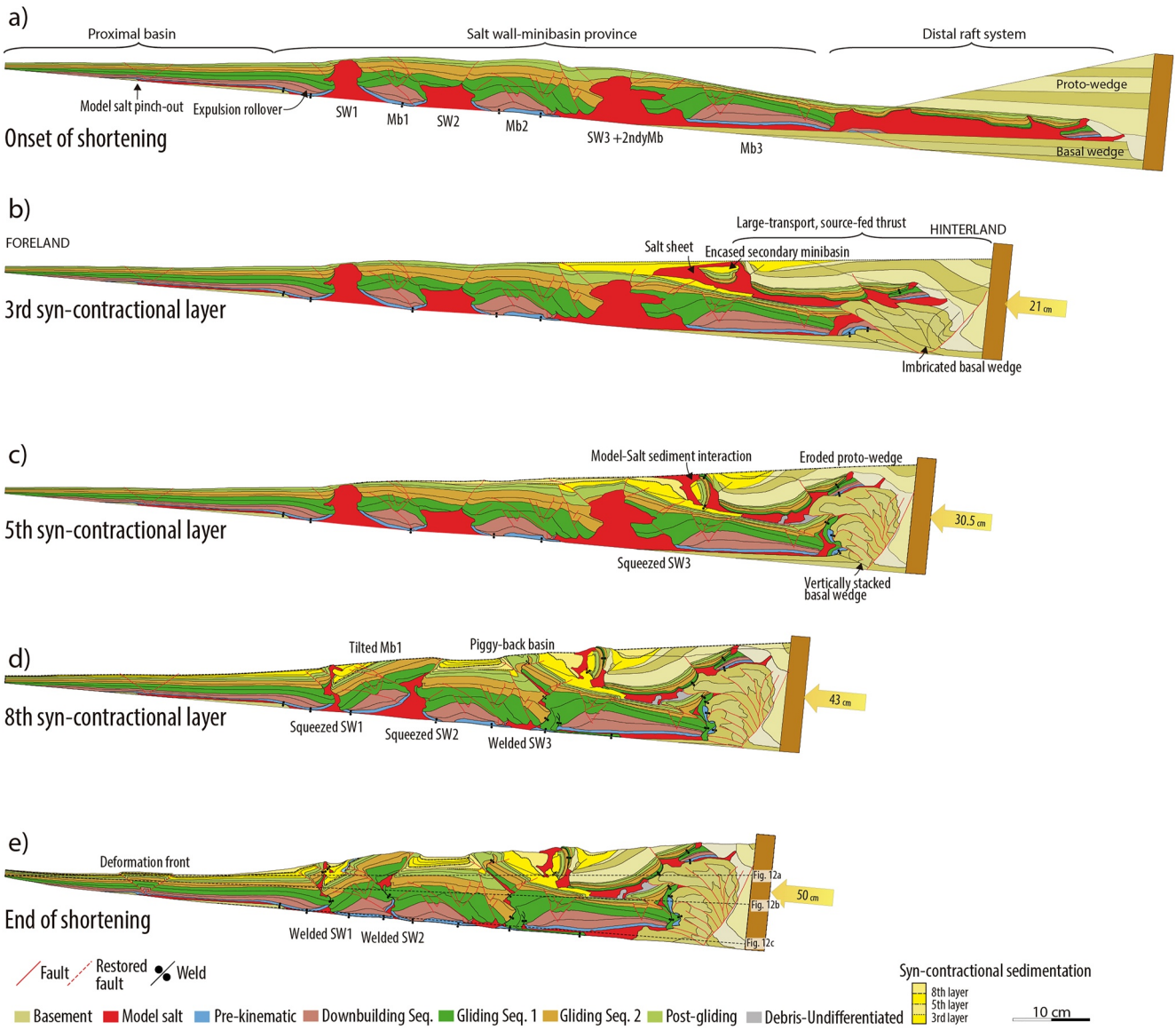

Figure 10. Evolution of Model 3 illustrated by the multi-stage restoration (a–d) of a representative cross-section of the model (e). Evolutionary stages coincide with those in Figure 9.

active. The previously-collapsed SW3 was squeezed, leading to diapir rise and roof arching and deformation of previous syn-contractional sedimentary basins (Figure 9c). Syn-contractional sedimentation prograded into the foreland and reached the position of SW2. After 43 cm of shortening, the model salt extrusion along the proto-wedge decreased (Figure 9d). SW2 was squeezed resulting in the growth of a significant relief above the regional erosion level. SW1 was also squeezed leading to model salt piercement and extrusion. A piggyback basin form behind such relief (Figure 9d). Syn-contractional sedimentation reached the distal foreland basin. It was not until shortly before the end of experiment that deformation reached the distal pinch-out where a box-fold popped-up (Figure 9e).

The evolution of Model 3 at depth is illustrated here by means of the multi-stage restoration of one representative section of the experiment (Figure 10). As in previous models, the rifted margin stage depicts similar tectonostratigraphic and structural features (Figure 10a): the proximal basin, the salt wall-minibasin province having a taller SW1 and a wider Mb3 than Model 2, and the distal raft system where salt accumulation exceeds the one shown in Model 2. Upon shortening, the basal wedge grew as a double verging imbricate system. Above the basal wedge

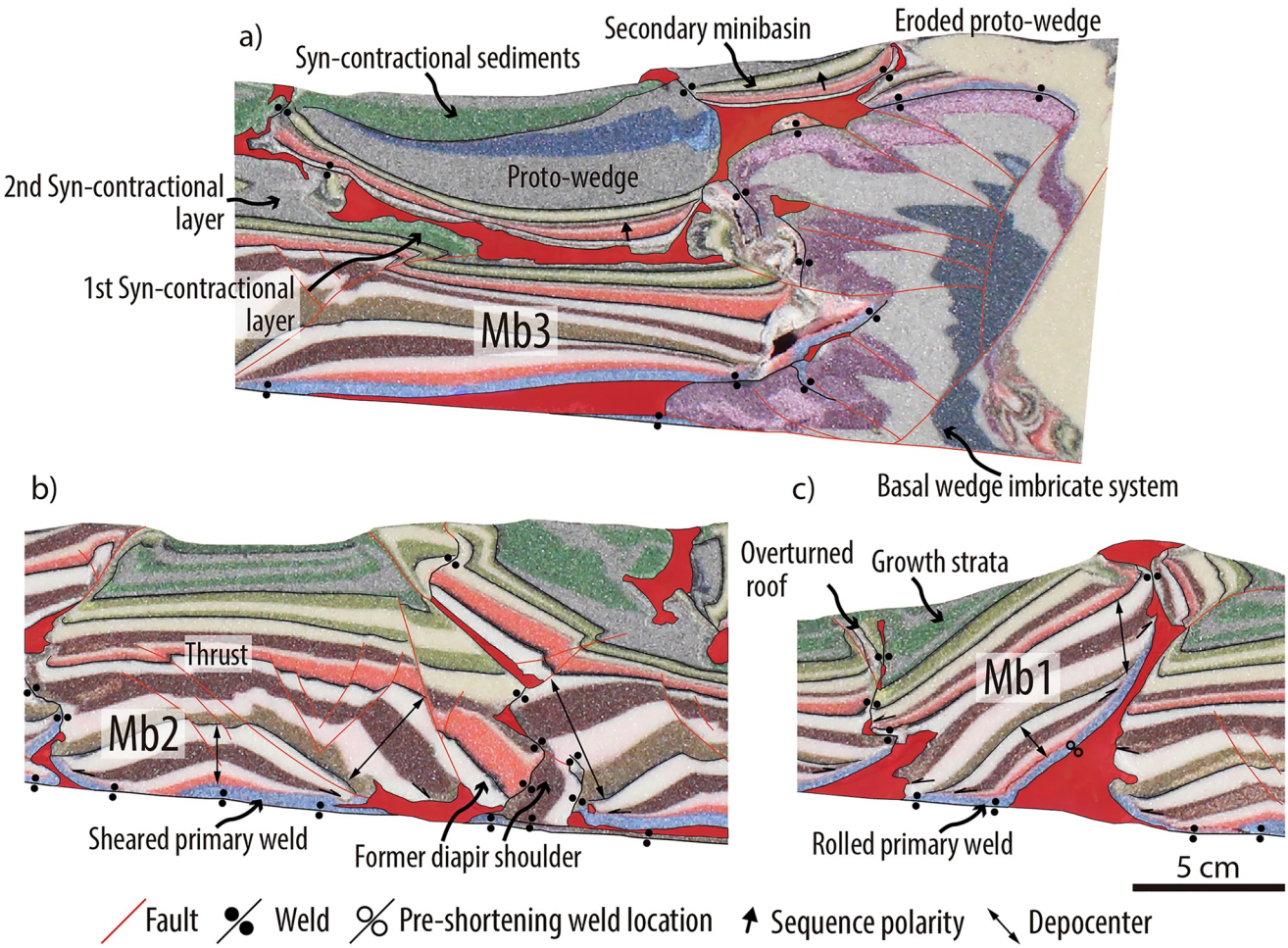

Figure 11. Representative close-ups of Model 3 showing (a) minibasin 3 and the basal wedge imbricate system, the deformed distal raft system and the proto-wedge, (b) minibasin 2 and salt wall 3 and (c) salt walls 1 and 2 and minibasin 1.

imbricate system and detached along the distal raft system salt accumulation, the proto-wedge advanced over Mb3 (Figure 10b). The model salt extruded from its toe, over syn-contractional layers, and formed a triangular model salt accumulation that hosted an encased secondary minibasin (Figure 10b). This configuration represents a large-transport, source-fed thrust (Jackson & Hudec, 2017). Model salt extrusion took place coevally with surface processes resulting in extruded model salt flowing over syn-contractional sediments (Figure 10b). Further shortening led to additional imbrication of the basal wedge that grew vertically and uplifted the proto-wedge which was consequently eroded (Figure 10c). At the same time, SW3 was squeezed and its roof arched. Later on, this SW3 was finally shut off and deformation transferred forwards leading to narrowing of SW2 and SW1 and tilting of Mb1, while in the hinterland the basal wedge kept on growing vertically (Figure 10d). Soon before the end of the experiment, SW2 and SW1 were completely welded and the deformation front moved forward to the model salt pinch-out (Figure 10e).

At the end of the experiment, the hinterland features a 11 cm tall thrust stack system involving the basal wedge (Figure 11a). The bounding surface of the thrust stack consists of a series of welds and salt remnants. On top of it, rafts and secondary minibasins represent the topographically highest elements of the orogenic wedge while most of the proto-wedge was eroded. In front of the thrust stack, the proto-wedge thrust over Mb3 and forms a large-transport, source-fed thrust (Figure 11a). In its footwall, the youngest syn-contractional sediments are thrusted and eventually deformed. Closure of SW3 led to an intricate boundary of welds and model salt remnants controlled by the inherited geometry of this wall, which was characterized by the presence of diapir shoulders, wings, extensional features and a roof variable in thickness (Figure 11b). Landwards, Mb2 preserved its original flat-lying turtle geometry and displays contractional features such as a landward-verging thrust and a sheared

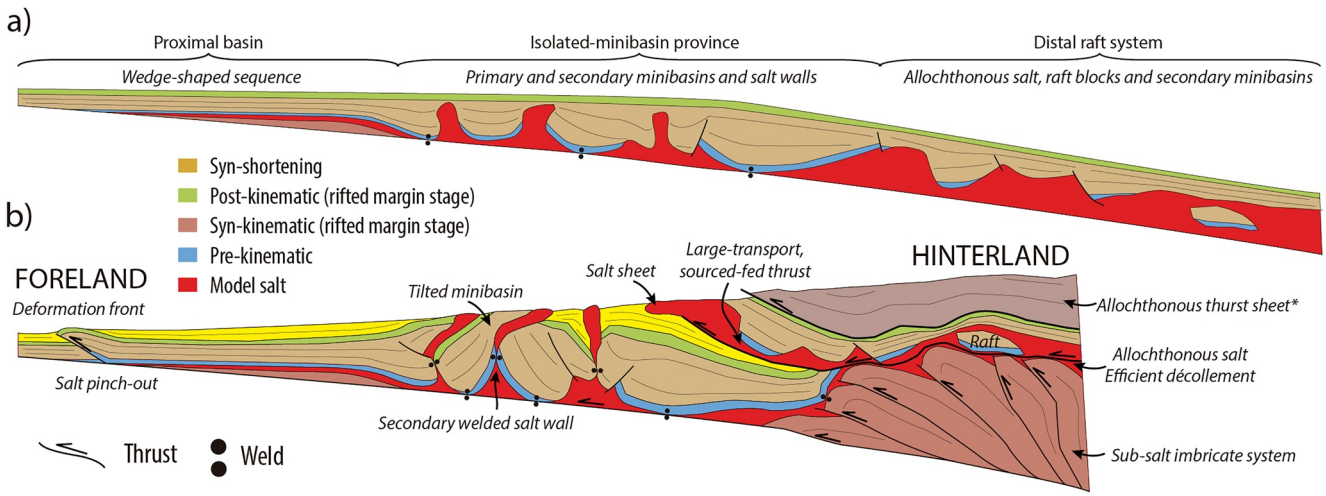

Figure 12. Sketched sections that summarize analog modeling results and illustrate how the rifted margin architectural elements (a) are incorporated into a fold-and-thrust belt (b).

primary weld (Figure 11b). Landward tilting of Mb1 attained 35° (Figure 11c). Forward tilting led to formation of syn-contractional growth sequences and onlap relationships (Figure 11c) and the migration of the original position of the primary weld forwards resulting in a rolled primary weld. Secondary welding of SW1 features a vertical weld where growth strata are directly in contact with the overturned roof sequence.

4. Discussion

4.1. Role of Inherited Salt-Related Rifted Margin Architecture and Propagation of Deformation

The overall salt-sediment architecture at the end of the rifted margin stage in all the models involves: a proximal basin, a salt wall-minibasin province and a distal raft system (Figures 4b, 7a, 10a, and 12a). Differences arise regarding the geometry of salt walls, in terms of their height and width and especially the architecture acquired after the collapse of SW3. Models 1 and 3 display a single salt wall flanked by wedge-shaped sedimentary sequences (Figures 4b and 10a), while Model 2 depicts a secondary minibasin flanked by two salt walls (Figure 7a). The raft system varies from consisting of a set of up to 4 rafts separated by model salt bodies with limited growth of secondary minibasins (Model 1, Figure 4b) to a wide model salt body with a limited number of rafts (Model 3, Figure 10a). The tectonostratigraphic architecture of the rifted margin salt-sediment system involved a set of relatively stronger bodies (i.e., minibasins and rafts) surrounded by weaker salt bodies (i.e., salt walls and salt sheets). The resulting geometry of the sedimentary infill is the opposite of a layer-cake configuration: abrupt thickness variations, condensed sequences, omitted stratigraphy, intricate stratigraphic contacts related to primary, secondary and tertiary welding, and allochthonous salt sheets and model salt being stratigraphically and mechanically in contact with all the involved stratigraphic units (from pre- to the post-kinematic).

Then, during shortening of the salt-bearing rifted system and as a general rule, contractional deformation is transferred landwards in a forward-stepping sequence and, to some extent, the orogenic wedge grew according to the critical taper theory (Dahlen, 1990). Initially, most of the shortening was accommodated by thrust stacking of the basal wedge and forward advance of the distal raft system and proto-wedge, then deformation moved to the salt wall-minibasin province and finally reached the distal model salt pinch-out.

The model salt in the distal raft system attained up to approximately 3 cm in thickness and represents a very effective décollement that decoupled contractional deformation in the basal wedge and the proto-wedge (Figure 12b). This is a common observation in those settings involving interbedded *décollement* levels (Couzens-Schultz et al., 2003; Pla et al., 2019; Santolaria et al., 2015). In Model 3 (Figures 10a and 10b), such *décollement* permitted the forward translation of the proto-wedge defining a large-transport, source-fed thrust that accounts for about 40% of the total shortening. Large-transport thrusts have been described in natural fold-and-thrust

belts involving salt *décollements* such as the Salt Range in Pakistan (Grelaud et al., 2002), the Quele Fault in the Kuqa Basin of NW China (Izquierdo-Llavall et al., 2018; Rowan, 2017), and the Chazuta thrust in the Sub-Andean zone of northern Peru (Borderie et al., 2019; Eude et al., 2015; Zamora et al., 2019, 2022). Mechanically, the occurrence of large-transport faults is favored by a thick and very effective, low yield-strength, or viscous layer, a sedimentary wedge on top of it (mechanically equivalent to our proto-wedge) and forward salt inflation (Borderie et al., 2019; Ferrer et al., 2022); characteristics that converge in our Models 2 and 3. Thick *décollements* yield a continuous feeding of the inflated salt in their hanging-wall that may eventually extrude along the front of these source-fed, large-transport thrusts, leading to additional salt sheets that may extend beyond the thrust front (Figure 10b). Section restoration is subject to some degree of uncertainty related to the definition of the hanging wall cutoff. The amount of shortening could be overestimated if the salt sheet is totally or partially considered as part of the advancing thrust sheet, for example, if the hanging-wall cut off is interpreted to be at the tip of the salt sheet. Or underestimated since the hanging-wall cut-off could be absent by erosion (Figure 12b). In Model 2, the distal basin model salt accumulation hosted small (3 cm wide) to large (15 cm wide) rafts and was capped by secondary minibasins. There, the large-transport thrust stands as an intricate system of imbricated rafts, secondary minibasins, source-expelled model salt and welds (Figure 8a). Yet, the proto-wedge appears as a stiff body, passively transported forwards, with little evidence of internal deformation.

After large-transport thrusting, deformation transferred to the salt wall-minibasin province. There, contractional deformation focusses on salt walls whereas minibasins are translated, jostled and eventually collided (Duffy et al., 2017, 2021) and rotated (Callot et al., 2016; Duffy et al., 2021; Ferrer, 2012; Rowan & Vendeville, 2006; Santolaria, Granado, et al., 2021) whilst broadly preserving their original architecture (Rowan & Vendeville, 2006). During salt wall squeezing, inherited roof thickness played a significant role. Thin roofs are easily pierced by uprising pressurized model salt leading to salt extrusion (Figures 6 and 9d) (e.g., Nilsen et al., 1995), whereas thick roofs promote arching or thrusting. In those salt walls with thicker roofs, thrust faults preferentially nucleate at the crest of salt walls, where the roof is relatively thinner or at the inflexion point between salt wall flanks and roofs (see red dashed lines in Figures 7a and 10a). In those cases where pressurized model salt could not pierce the cover and extrude, it was expelled landwards and downwards assisting in the forward tilting of Mb1 and the formation of rolled primary welds. This process of model salt deflation is described in detail in Dooley et al., 2009.

Squeezing results in salt wall closure and secondary welding (e.g., Nilsen et al., 1995; Vendeville & Nilsen, 1995; Rasmussen et al., 1998; Ferrer, 2012; Roma, Ferrer, et al., 2018; Santolaria, Ferrer, et al., 2021; this work). Squeezing of vertical salt walls flanked by trough-like minibasins results in relatively simple secondary welds, commonly localized along the maximum lateral expansion of minibasins (Duffy et al., 2021; Ferrer, 2012; Roma, Ferrer, et al., 2018; Rowan & Vendeville, 2006; Santolaria, Granado, et al., 2021). Conversely, in our models, the uneven inherited geometry of the salt walls and their flanks led to variable secondary weld geometries and tectonostratigraphic relations: interdigitated diapir shoulders and wings (Figures 11c and 11b), pinched secondary minibasins (Figure 8b) and welds that put in contact younger sequences with the oldest layers of the modeling package (Figure 8c). Such structural and tectonostratigraphic configuration could be puzzling in natural fold-and-thrust belts if a layer-cake stratigraphy is assumed. Finally, deformation reached the foreland in the form of a box-fold nucleated at the distal model salt pinch-out (Figure 12b).

Salt accumulations commonly localize deformation due to the inherent weakness of it (Weijermars et al., 1993; Vendeville & Nilsen, 1995; Letouzey et al., 1995; Rowan & Vendeville, 2006; Dooley et al., 2009; Ferrer, 2012; Duffy et al., 2018; Roma, Ferrer, et al., 2018; Roma, Vidal-Royo, et al., 2018; Granado et al., 2021; Santolaria, Ferrer, et al., 2021, Santolaria, Granado, et al., 2021). As observed in other analog modeling programs, salt bodies represent weak discontinuities within the modeling sand package that absorb most of the horizontal contraction (e.g., Koyi, 1988; Vendeville & Nilsen, 1995; Nilsen et al., 1995; Roca et al., 2006; Rowan & Vendeville, 2006; Callot et al., 2012; Ferrer, 2012; Duffy et al., 2018, 2021; Santolaria, Ferrer, et al., 2021; Santolaria, Granado, et al., 2021; among others). All in all, our results evidence the role played by the inherited passive margin architecture and especially the distribution of the model salt: (a) thick, distal raft model salt promote decoupling of the sub- and supra-salt deformation and the formation of a large-transport, source fed-thrust, (b) in the diapir-minibasin province, salt-walls localize deformation and account for most of the shortening accommodated in this area and (c) the distal model salt pinch-out control the deformation in the foreland.

4.2. Surface Processes During Shortening

It is well known that syn-contractional erosion and sedimentation delays forward propagation of deformation since surface processes reduce the average slope of the orogenic wedge and hinterland structures keep growing in order to reach the critical taper angle (Boyer, 1995; Graveleau et al., 2012; Huiqi et al., 1992; Simpson, 2006; Stockmal et al., 2007; Storti & McClay, 1995; Wu & McClay, 2011). Our models are not an exception, and this delay is especially evident in the reactivation of proximal salt walls (SW1 and 2) that occurred after 56% of shortening in Model 2 (no surface processes) and later on, after 60% of shortening, in Model 3 (surface processes). Similarly, the reactivation of the distal pinch-out that occurred after 83% of shortening in Model 2 and after 90.5% of shortening, in Model 3. According to the critical taper theory, mass redistribution caused by erosion and sedimentation tend to reduce the taper and consequently the wedge has to adapt and return to critical equilibrium conditions (Dahlen & Suppe, 1988; Davis et al., 1983; Graveleau et al., 2012; Mugnier et al., 1997). The more pronounced vertical growth of the basal wedge imbricate system in Model 3 (12 cm; Figure 11a) with respect to Model 2 (6 cm; Figure 8a) is a direct response of the basal wedge to the erosion occurring on top of the proto-wedge.

Syn-tectonic sedimentation also exerts a first-order control on the wavelength and the number of structures since the thicker the cover the larger the structural spacing (Costa & Vendeville, 2002; Pla et al., 2019). This concept fully applies in those settings considering layer-cake sedimentary sequences. In our case, the inherited salt-sediment architecture prevails as a controlling factor of the distribution of deformation as the location of salt bodies determines the position of later contractional features (as discussed above). Syn-contractional sediments interact with the growing wedge and record contractional deformation of the salt-sediment system. In the hinterland, young syn-contractional sediments advance together with a large-transport thrust while older syn-contractional layers are thrusted by it (Figure 11a). It is at the tip of the large-transport thrust where extruding model salt interacts with syn-contractional sediments. Extruded model salt and advancing salt sheets partially cover and bulldoze syn-contractional sediments while younger sediments are deposited on them. This results in an intricate geometry including millimeter-scale thrusts and syn-contractional sediment debris that prevents a reliable interpretation of the structure (Figure 11b). On top of those untilted minibasins, syn-contractional sedimentation sequences display a vertical stack of nearly horizontal, and constant-thickness layers (Figure 11b). Toward the edges of these sand packages, deformation intensifies and includes growth strata characterized by overturned layers. This deformation extends up to 2 cm away from thrusts whilst involving the roof of squeezed salt walls (Figure 11b). These relatively short wavelength growth strata differ from what is found on top of tilted minibasins. There, growth strata record the progressive tilting of minibasin and therefore cover its entire length (Figure 11c). Such differences can be useful templates when interpreting syn-contractional sedimentation sequences and architectures in natural minibasin-provinces incorporated in fold-and-thrust belts.

4.3. Where Does the Salt Go? Original Model Salt Versus Model Salt After Shortening

As introduced early on and as shown by our results, a common question when analyzing salt-detached fold-and-thrust belts is what is the original amount of salt prior to shortening since contractional structures tend to show limited amounts of it (Calvín et al., 2018; Granado et al., 2019). Such question is commonly fostered by the low preservation potential of (soluble) evaporitic formations in temperate humid climates, which tend to render evaporite formations to rubble zones and *block-in-matrix* mélange fabrics (e.g., Festa et al., 2010), particularly when subjected to deformation and fluid circulation (i.e., *rauhwacke*, in Warren, 2016, p. 656). Subsequently, salt remnants may only occur as the insoluble residue of the original layered evaporitic sequence, such as the Neoproterozoic Callanna Gp. breccias of the Australian Flinder Ranges (Hearon et al., 2015), or the Roan Gp. of the Central African Copperbelt (Selley et al., 2018) or represented in the Haselgebirge Fm. in the Northern Calcareous Alps (Leitner & Spötl, 2017). Salt would be exceptionally preserved on active fold-and-thrust belt (i.e., where salt is actively being extruded) and in particular, where arid climate conditions prevail (i.e., Zagros of Iran, Talbot, 1988; Talbot et al., 2000; Snidero et al., 2019, 2020).

In contractional systems, salt is either preserved as squeezed diapirs (e.g., Callot et al., 2012), along thrust welds (e.g., Hossack, 1995; Vidal-Royo et al., 2021), at the base of the thrust sheets (e.g., Davis & Engelder, 1985; Hudec & Jackson, 2006), and under certain conditions, as allochthonous salt sheets (e.g., Hudec & Jackson, 2006; Rowan, 2017). Upon shortening, the existence and rejuvenation of pre-existing salt bodies represent efficient channels to evacuate salt from the bodies themselves and the source layer to the surface (Callot et al., 2012;

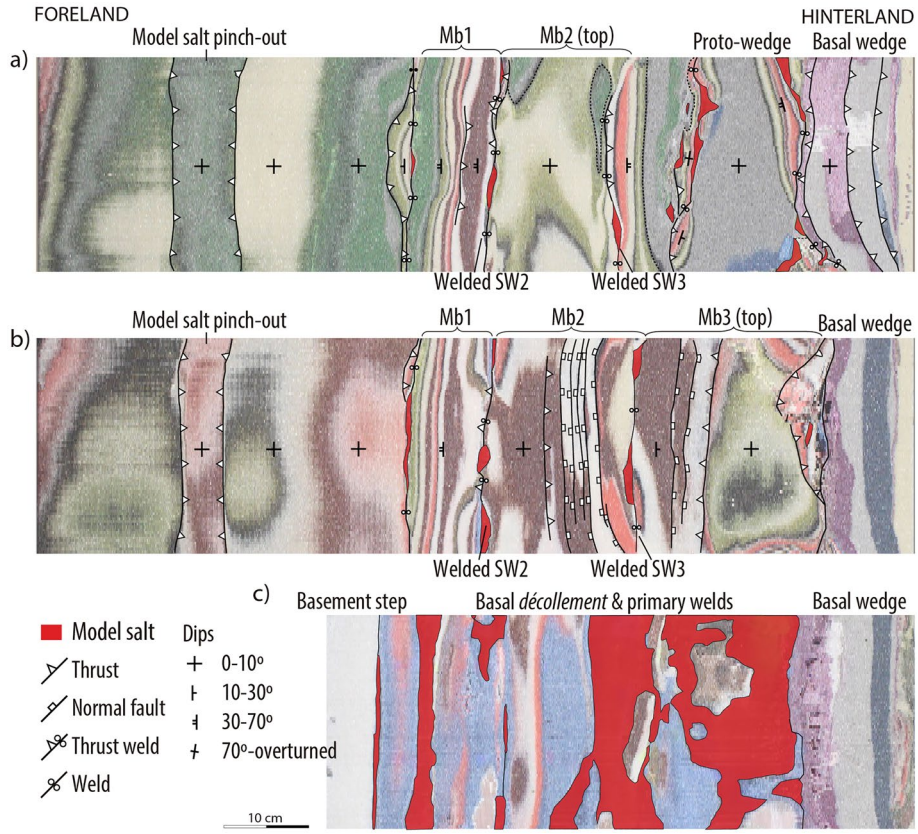

Figure 13. Interpreted depth and oblique slices of Model 3. (a) Depth slice 3 mm below the regional level of the foreland, (b) hinterland tilted intermediate slice, (c) deep slice, 3 mm above the basal plate and nearly parallel to it. See Figure 10e for location.

Ferrer, 2012; Nilsen et al., 1995; Roca et al., 2006; Rowan & Vendeville, 2006; Santolaria, Ferrer, et al., 2021). Source-fed thrusts are also potential paths for the salt to evacuate and reach the surface. All in all, the amount of extruded salt in such contractional systems may positively correlate with the number and dimensions of evacuation channels (i.e., salt bodies) and the amount of shortening. Factors that prevent the shut-off of salt bodies, such as intra-salt sediment bodies (Duffy et al., 2017) roof blocks or encased minibasins (this study), could halt extrusion and promote the preservation of salt within the salt-sediment system. Our analog models had several potential evacuation paths: salt walls and the large-transport, source-fed thrust. After shortening, model salt represented about 5% of the salt-sediment system even though it attained about 20% before contraction. This represents a model salt loss of about 75%. Section restoration of salt-related contractional systems is always complicated (Granado et al., 2019; Roma, Vidal-Royo, et al., 2018; Rowan & Ratliff, 2012; Santolaria, Granado, et al., 2021) since, for example, it is difficult to assess the amount of shortening accommodated by pre-existing salt bodies where cryptic deformation occurred (e.g., Jackson et al., 2015). Besides, restorations become even more challenging if present-day salt-sediment ratios differ from the configuration prior to shortening.

Virtual depth and oblique slices of Model 3 (Figure 13) illustrate from top to bottom (Figures 13a–13c, respectively) the common misconception about the absence, and hence the role, of salt in many fold-and-thrust belts. Model salt is preserved at the upper reaches of squeezed salt walls (Figures 13a and 13b), and preferentially accumulated in the deepest parts of the system, such as diapir pedestals and as thin thrust welds at the base of welded minibasins (Figure 13c). These virtual sections also show the lateral variability of preserved salt along thrust welds, which have a significant impact into the connectivity across minibasins. Once subjected to erosion, this kind of fold-and-thrust belts may show very little evidence of salt if only judged from the salt preservation record. Regarding these depth and oblique slices as geological maps, it is evident that non-evaporitic rocks (i.e., colored sand in our models) largely dominates. For these reasons, the most appropriate approach to understand the role of salt in the evolution of fold-and-thrust belts developed from salt-bearing rifted margins is to understand the

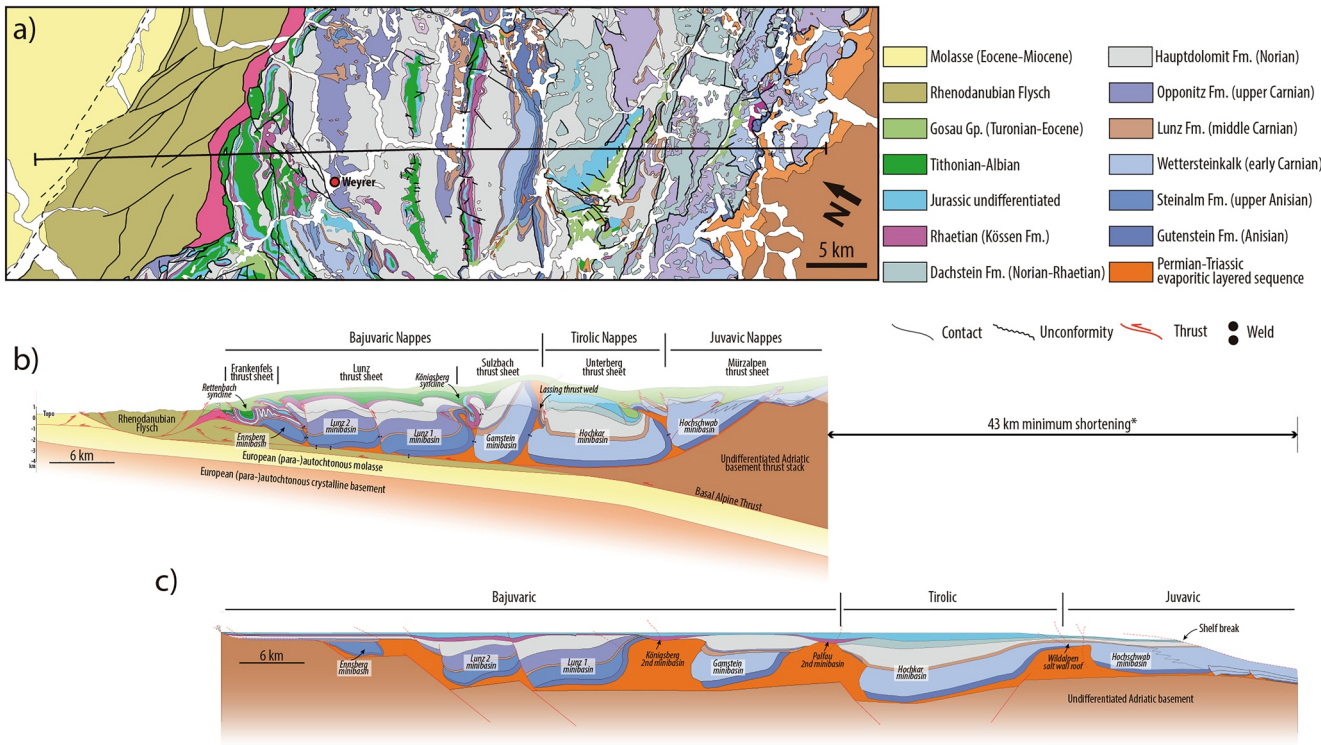

Figure 14. (a) Geological map of the study area based on the 1:200.000 geological map of Niederösterreich (Lower Austria) modified from Schnabel et al. (2002). (b) NW–SE cross-section through the eastern Northern Calcareous Alps and its restoration. *Note that minimum calculated shortening represents just the shortening accommodated by thrust imbrication, minibasins tilting and salt wall closing; horizontal displacement on top of the European (para)-allochthonous molasse is not considered.

post-salt stratigraphic record, its facies and thickness distribution, its age as well as its contact with salt remnants, rather than on the salt itself.

4.4. Natural Case Studies

4.4.1. The Northern Calcareous Alps of Austria

The Northern Calcareous Alps constitute a N-NW-directed salt-detached fold-and-thrust belt (Linzer et al., 1995; Mandl, 2000). Its structure consists of ENE-WSW–striking thrust sheets, which from north to south have been grouped into three major units, namely the Bajuvaric, Tirolic-Noric, and Juvavic nappe systems, respectively (i.e., Bajuvaricum, Tirolicum, Juvavicum *sensu* Hahn, 1912, 1913). Each of these three large units is characterized by a distinct stratigraphy in terms of facies and thicknesses, which overall define an approximate north-to-south deepening trend for the Neo-Tethys margin (Mandl, 2000; Tollmann, 1985, 1987). Additional distal units, such as Hallstatt and Meliatta, are constituted by deeper water facies deposited on the distal domain of the Neo-Tethyan margin, since about Ladinian times (Mandl, 2000). The thickest stratigraphic section occurs in the central parts of the fold-and-thrust belt (i.e., in the Tirolic-Noric nappes, and the southern Bajuvaric nappe), where the Triassic units alone may reach vertical thicknesses in excess of 5 km (Strauss et al., 2021a, 2021b; Granado et al., 2021, Figure 14). Thinner stratigraphic successions occur to the north (i.e., the northern Bajuvaric nappes), and to the south (i.e., the Juvavic nappes). Such differences in stratigraphic thickness have also associated strong changes in structural wavelengths and structural styles (Frisch & Gawlick, 2003; Mandl, 2000). The archetypal structural styles of the Northern Calcareous Alps include large panels of overturned stratigraphy, and steep mechanical contacts marked by severely deformed evaporites that can either repeat or omit significant parts of the stratigraphic sequence. Other parts of this fold-and-thrust belt conform to classical thrust contacts bringing older stratigraphy onto younger stratigraphy and constituting thrust sheets of significant lateral continuity (i.e., tens of kilometers; see Granado et al., 2021). Such complex structural styles of the Northern Calcareous Alps were interpreted as resulting from strong out of sequence thrusting and Cenozoic strike-slip overprinting a typical

fold-and-thrust belt (e.g., Linzer et al., 1995, 1997; Frisch & Gawlick, 2003, amongst many others). However, more recent works have proven the importance of salt tectonics (i.e., initiated during the rifted margin stage) in controlling such archetypal structural styles (Granado et al., 2019; Strauss et al., 2021a, 2021b).

In the following, we present a new cross-section across the western limit of the eastern Northern Calcareous Alps (Figures 14a and 14b), and its restoration to the base of the Jurassic (Figure 14c), previous to the onset of Alpine convergence. The section crosses the full stretch of the Northern Calcareous Alps, and completes, to the north and south, the original balanced section across the Gamsstein minibasin, where salt tectonics in the Northern Calcareous Alps were defined for the first time (i.e., Granado et al., 2019). The new section depicts large thrust sheets involving thick carbonate minibasins bound by subvertical welds, thrust welds, and thrust slices involving thinner stratigraphic successions. The complex structural styles and heterogeneous stratigraphic record of the Northern Calcareous Alps renders significant uncertainty for balanced cross-section construction, particularly in the sub-thrust zones and below the apparent subtractive mechanical contacts. Here, we demonstrate by means of balanced cross-section construction, restoration, and structural templates derived from our sandbox models, that all these complex structural styles are the result of the contraction of Triassic and Jurassic minibasins originally flanked by km-long salt walls developed by downbuilding and dominant gliding on the northern Neo-Tethys salt-bearing rifted margin.

4.4.2. A New Cross-Section Through the Eastern Northern Calcareous Alps

Our new cross-section shows that the Northern Calcareous fold-and-thrust belt have been completely detached from their original Adriatic rifted basement, where the salt was originally deposited, as a result of Alpine convergence. Exploration well control indicates the presence of the Rhenodanubian Flysch (i.e., the Alpine suture between Adria and Europe continental lithospheres), the Alpine Molasse and Mesozoic sediments deposited on the European crystalline basement beneath the basal décollement of the Northern Calcareous Alps (Wessely, 1992, 2006) (European (para-)autochthonous units, Figure 14b). From south to north, the Mürzalpen thrust sheet of the Juvavic nappes and the Unterberg thrust sheet of the Tirolic-Noric nappes include a complete Middle to Upper Triassic succession and undifferentiated Jurassic strata, unconformably overlaid by the synorogenic Turonian to Paleocene succession of the Gosau Gp. The Gosau Gp. synorogenic deposits are preserved on the footwall to several thrust and back-thrusts, indicating the out-of-sequence reactivation of these structures. The Mürzalpen and the Unterberg thrust sheets are soled and detached along the Permian evaporites; however, their *ca.* 30° northward tilt indicates the involvement of the Adriatic basement in a hinterland thrust stack, in a similar fashion to other fold-and-thrust belts (Boyer & Elliot, 1982; Muñoz et al., 2018) and the hinterland wedge of our sandbox models (compare Figures 8a, 11a, and 14b). The contact between the Juvavic and the Tirolic-Noric nappes (Figure 14b) has been traditionally interpreted as an Oligocene-Miocene left-lateral strike-slip fault with several tens of kilometers of displacement along strike (i.e., the Salzach-Ennstal-Mariazell-Puchberg fault system, or SEMP *sensu* Decker & Peresson, 1996; Linzer et al., 1997). Our section and its restoration show that the so-called SEMP fault is in fact a squeezed salt wall, with a diapir roof of thin stratigraphy imbricated in a flower-like structure (Figure 14b). The results from our analog modeling also show very similar thrust imbricates (i.e., pop-up like) form by contraction exclusively (Figures 8c and 11b, c), with no displacements along strike produced under any strike-slip regional stress field. Careful inspection of the regional geological maps (Schnabel et al., 2002) show that the so-called SEMP fault in the study area shows no displacement along strike at all, without any offset of geological markers.

Farther north in the cross-section, the contact between the Bajuvaric and Tirolic-Noric nappes is represented by the Lassing thrust weld (Granado et al., 2019). The contact is represented by severely deformed evaporites, and brings the ca. 50° forelandward-tilted Sulzbach thrust sheet (i.e., the Gamsstein minibasin; Figure 14b), into contact with the Unterberg thrust sheet. The Gamsstein minibasin is of key relevance for cross-section construction since its tilting provides a complete stratigraphic section from the Permian salt to the to Lower Cretaceous syn-orogenic section. In our Models 2 and 3, Mb1 also underwent forelandward tilting upon contraction, most of such tilting accommodated by a combination of salt wall squeezing, diapir roof-arching, and back-thrusting, with or without syn-orogenic sedimentation and erosion (Figure 14b).

The Sulzbach thrust sheet is bound northwards to the Lunz thrust sheet across the tightly folded north-vergent and inclined Königsberg syncline (Figure 14b). The Königsberg syncline also displays a curved axial surface, and is represented by a thin Norian succession, overlain by a depocenter of Rhaetian and Jurassic units, and Lower

Cretaceous syn-orogenic strata (Figure 14b). Further north, the Lunz thrust sheet is characterized by two large depocenters that display a moderately-folded and complete Middle to Upper Triassic succession.

The contact between the Lunz thrust sheet and the northerly Frankenfels thrust sheet is constituted by a steeply south-dipping imbricate of Upper Triassic units. The imbricate displays a thinner Upper Triassic succession than in the southern Bajuvaric and Tirolic-Noric nappes. The structure and stratigraphic succession of the Frankenfels thrust sheet displays a significant change to those units to the south and provides key constraints for cross-sections construction. In more detail: tight transported detachment folds involve a relatively thin (*ca.* 650m thick) Upper Triassic stratigraphic succession, which include the upper Carnian Opponitz Fm., the Norian Hauptdolomit Fm., the Rhaetian Kössen Fm., and undifferentiated Jurassic on top. In addition, an 800-m-thick uppermost Jurassic to mid Cretaceous growth syncline (i.e., the Rettenbach syncline, Figure 14b) in the Frankenfels is also present. These two features (tight anticlines and synclines, and a growth syncline) suggest an efficient décollement level located in a shallower position than that of the Lunz thrust sheet. The best mechanical candidate is the evaporitic-carbonatic Opponitz Fm. In addition, the Rettenbach growth syncline (Figure 14b) indicates a change in the structural elevation immediately to the south. These features indicate the location of a thrust ramp from the Permian into the upper Carnian evaporitic levels, as already suggested by Linzer et al. (1995). The growth syncline developed immediately ahead of the frontal culmination wall of the basal décollement in the Permian evaporites involving the complete Middle to Upper Triassic section. The south dipping back limb of this thrust sheet can be taken as a proxy to the dip of the ramp linking the Permian and the upper Carnian *décollements*.

4.4.3. Restoration of the Cross-Section and Comparison to Analog Models

Restoration of the complete regional N-S cross-section to the base of the Jurassic (Figure 14c) depicts a series of Middle to Upper Triassic primary salt-related minibasins, namely the Ennsberg, Lunz 1, Lunz 2, Gamstein, Hochkar, and Hochschwab. The primary minibasins are flanked by collapsed salt walls, infilled by latest Triassic to latest Jurassic secondary minibasins (Figure 14c), namely the Königsberg minibasin in between the Lunz 2 and the Gamstein primary minibasins, the Palfau minibasin (mostly eroded, but originally developed between the Gamstein and the Hochkar primary minibasins), and the Wildalpen minibasin (also mostly eroded, but originally developed between the Hochkar and the Hochshwab primary minibasins).

Our cross-section restoration to the base of the Jurassic indicates that upon Alpine convergence salt walls were squeezed and shut off, producing structurally complex relationships such as: large panels of overturned stratigraphy, and steep mechanical contacts that can either repeat or omit significant parts of the stratigraphic sequence. In the presented section of the Northern Calcareous Alps, the overall structure corresponds to a contractional salt wall-minibasin province. Squeezed salt walls are represented by subvertical secondary wells and thrust wells that mark the main thrust sheet boundaries, such as those in between the Lunz and the Frankenfels thrust sheets, the contact between the Bajuvaric and the Tirolic-Noric thrust sheets, and the former with the Juvavic thrust sheets. Some of these contacts appear as secondary salt welds in between flat-lying minibasins (i.e., compare contact of Mb 2 in models 2 and 3 with the Lunz 1 and Lunz 2 minibasins, or the contact in between the Hockar and Hochschwab minibasin in the Tirolic-Noric and Juvavic boundary; Figures 7b and 8b for model 2, and 10e and 11b for model 3). Other mechanical contacts take place across tilted minibasins and (back-)thrust welds (i.e., compare the Sulzbach thrust sheet in Figure 14c, with the forward tilted Mb1 in models 2 and 3, in Figures 7, 8c, and 11c).

Squeezing of subvertical salt walls flanking primary minibasins, and the imbrication of diapir roofs provide an alternative, geometrically and mechanically consistent explanation for the previously interpreted flower structures related to regional strike slip tectonics. Examples of these can be observed in the regional section and its structural restoration. In fact, our proposed model involving the contractional reactivation of a salt wall-minibasin province provides an alternative explanation that is internally consistent and restorable in cross-section and map view, and moreover, is capable of harmonizing the structural styles, the fold-and-thrust-belt kinematics as well as the Middle to Upper Triassic stratigraphic development, which has never been fully considered by previous authors supportive of strike-slip tectonics in the area. Despite the rare occurrence of Permian evaporites along the presented section of the Northern Calcareous Alps the restored section shows massive accumulations of salt in between minibasins. Such accumulations may have exceeded a width of 7 km and a height of 4 km previous to Alpine convergence (Figure 14c). As proved by lack of abundant model salt at the end of shortening in our analog modeling results, the rare occurrence of Permian evaporites in map view and in the section does not discard salt tectonics in this (and other) area of the Northern Calcareous Alps.

5. Concluding Remarks

Our experimental models illustrate how the inherited architecture of the salt-bearing rifted margin plays a major role on controlling structural styles when incorporating the margin into a fold-and-thrust belt system and how surface processes impact the kinematics during mountain building.

In our models, at the end of the rifted margin stage, the combination of downbuilding followed by dominant gliding leads to a margin architecture that displays a seaward thickening proximal basin that terminates in an expulsion rollover, a salt wall-minibasin province and, beyond the shelf-break, a distal raft system. The salt wall-minibasin province includes primary and secondary minibasins, turtle structures, salt walls and collapsed salt walls. The distal raft system is characterized by the presence of a large, allochthonous accumulation of model salt hosting several raft blocks.

Due to the low-strength model salt, allochthonous model salt sheets emplaced at the distal raft system serve as an efficient *décollement* that promotes large-transport thrusting since the initiation of shortening. In salt wall-minibasin provinces, however, most of the shortening is accommodated by squeezing of salt walls. There, minibasins are transported forward and/or tilted, while flanking salt walls shut off forming secondary wells. With additional contraction, thrusts nucleate from secondary welds and salt wings.

Analog models show that the elements inherited from the rifted margin stage play an active role during mountain building at different scales: (a) allochthonous salt sheets emplaced during dominant gliding become a large-transport source-fed thrust systems; (b) salt walls localize deformation, while salt wings promote thrusting. Apart from the structural imprint, some stratigraphic relationships acquired during the evolution of the salt system are also incorporated and even reworked during orogenic wedging. These may include omission of stratigraphy, condensed sequences, truncations or repetitions whose understanding may be puzzling in natural fold-and-thrust belts when a layer-cake stratigraphy is anticipated.

The best practice approach for a clearer and predictive understanding of geometries and kinematics of salt-influenced fold-and-thrust belt resides in the inherited salt-related rifted margin stratigraphy involved, and not in the salt itself, since salt is generally poorly preserved in the stratigraphic record. Only active fold-and-thrust belts in submarine systems (South Atlantic, Gulf of Mexico), or in arid climate conditions (Zagros, Kuqa), allow the preservation of salt.

Surface processes, broadly erosion in the hinterland and deposition in the foreland or localized piggy-back basins, delays the forward propagation of deformation. Erosion of the hinterland promotes a higher thrust stacking of pre-salt units so that the former raft basin is largely uplifted and exposed. Stacking of basement thrust sheet. also allow the emplacement of the deep-water raft system above the former proximal domain of the rifted margin (i.e., on the salt wall-minibasin province), a process that has been elsewhere described in natural systems (Tavani et al., 2021). In the foreland, syn-contractional sediments interact with extruding model salt and record minibasin tilting.

Our models also show how shortening and erosion efficiently promoted the evacuation of model salt to the surface through former (i.e., long-lived diapirs of the salt wall-minibasin province) or newly formed salt fountains, formed by emergent source-fed thrust systems and erosion of their tips. In nature, under non-arid conditions, extruded salt to the surface may rapidly dissolve. Consequently, in a natural fold-and-thrust belt, the ratio between remaining versus original salt would be very low. The lack of abundant remnant salt units has been used as a counter argument against the influence of salt tectonics in fold-and-thrust belts. Our models provide a likely explanation to justify the lack of salt in these settings.

The role of salt tectonics in the Northern Calcareous Alps has been gaining acceptance as result of detailed geological mapping, cross-section construction and structural restorations, in addition to supportive works on rifted margin subsidence analysis. The structural and stratigraphic templates obtained by analog modeling have been key to better understand, and to propose an evolutionary model for the Northern Calcareous Alps shelf as a salt wall minibasin province. Our modeling approach and the obtained results, strongly support and provide insightful templates for refining structural and stratigraphic uncertainties. The key role of salt tectonics in the Northern Calcareous Alps is therefore, unequivocal.

Data Availability Statement

The uninterpreted sections of the models showed in Figures 4, 7b, and 10e are available in the "Dipòsit Digital," the open digital repository of the Universitat de Barcelona, in the following link: https://dataverse.csuc.cat/dataset.xhtml?persistentId=doi:10.34810/data510. Doi: https://doi.org/10.34810/data51.

Acknowledgments
This work is a contribution of the Institut de Recerca Geomodels (Universitat de Barcelona). This work stems from an industry collaboration with OMV E&P GmbH through project *Analogue modelling of Salt Tectonics*—FBG311629. The authors acknowledge the financial support of the research project Structure and Deformation of Salt-bearing Rifted Margins (SABREM), PID2020-117598GB-I00, funded by MCIN/AEI/11.13039/501110011133. The experimental program was executed at the GEOMODELS Analogue Modelling Laboratory at the University of Barcelona supported by a Scientific Infrastructure Grant (UNBA08-4E-006) provided by the European Regional Development Fund of the Ministerio de Ciencia e Innovación of the Spanish Government. Petroleum Experts are also acknowledged for providing Move software. Finally, the authors thank Leo M. Pichel and an anonymous reviewer for their constructive revisions that helped us to improve the manuscript.

References

Adam, J., & Krezsek, C. (2012). Basin-scale salt tectonic processes of the Laurentian Basin, Eastern Canada: Insights from integrated regional 2D seismic interpretation and 4D physical experiments. In G. I. Alsop, S. G. Archer, A. J. Hartley, N. T. Grant, & R. Hodgkinson (Eds.), *Salt tectonics, sediments and prospectivity* (Vol. 363, pp. 331–360). Geological Society of London. Special Publications. https://doi.org/10.1144/SP363.15

Adam, J., Urai, J., Wieneke, B., Oncken, O., Pfeiffer, K., Kukowski, N., et al. (2005). Shear localisation and strain distribution during tectonic faulting - New insights from granular flow experiments and high-resolution optical image correlation techniques. *Journal of Structural Geology*, *27*(2), 283–301. https://doi.org/10.1016/j.jsg.2004.08.008

Aslanian, D., Moulin, M., Olivet, J. L., Unternehr, P., Matias, L., Bache, F., et al. (2009). Brazilian and African passive margins of the central segment of the South Atlantic Ocean: Kinematic constraints. In G. Péron-Pinvidic, J. Van Wijk, D. J. Shillington, & L. Gernigon (Eds.), *Role of magmatism in continental lithosphere extension continental lithosphere extension*, *Tectonophysics* (Vol. *468*, pp. 98–112). https://doi.org/10.1016/j.tecto.2008.12.016

Baker, D. M., Lillie, R. J., Yeats, R. S., Johnson, G. D., Yousuf, M., & Zamin, A. S. H. (1988). Development of the Himalayan frontal thrust zone: Salt range, Pakistan. *Geology*, *16*(1), 3–7. https://doi.org/10.1130/0091-7613(1988)016<0003:dothft>2.3.co;2

Beamud, E., Muñoz, J. A., Fitzgerald, P. G., Baldwin, S. L., Garcés, M., Cabrera, L., & Metcalf, J. R. (2011). Magnetostratigraphy and detrital apatite fission track thermochronology in syntectonic conglomerates: Constraints on the exhumation of the South-Central Pyrenees. *Basin Research*, *23*(3), 309–331. https://doi.org/10.1111/j.1365-2117.2010.00492.x

Blaich, O. A., Faleide, J. I., & Tsikalas, F. (2011). Crustal breakup and continent-ocean transition at South Atlantic conjugate margins. *Journal of Geophysical Research*, *116*(B1), B01402. https://doi.org/10.1029/2010jb007686

Bonini, M. (2003). Detachment folding, fold amplification, and diapirism in thrust wedge experiments. *Tectonics*, *22*(6), 1065–1103. https://doi.org/10.1029/2002tc001458

Borderie, S., Vendeville, B. C., Graveleau, F., Witt, C., Dubois, P., Baby, P., & Calderon, Y. (2019). Analogue modeling of large-transport thrust faults in evaporites-floored basins: Example of the Chazuta thrust in the Huallaga basin, Peru. *Journal of Structural Geology*, *123*, 1–17. https://doi.org/10.1016/j.jsg.2019.03.002

Boyer, S. E. (1995). Sedimentary basin taper as a factor controlling the geometry and advance of thrust belts. *American Journal of Science*, *295*(10), 1220–1254. https://doi.org/10.2475/ajs.295.10.1220

Boyer, S. R., & Elliot, D. (1982). Thrust systems. *The American Association of Petroleum Geologists Bulletin*, *66*, 1196–1230.

Bronner, A., Sauter, D., Manatschal, G., Peron-Pinvidic, G., & Munschy, M. (2011). Magmatic breakup as an explanation for magnetic anomalies at magma-poor rifted margins. *Magmatic breakup as an explanation for magnetic anomalies at magma-poor rifted margins Nature Geoscience*, *4*(8), 549–553. https://doi.org/10.1038/ngeo1201

Brun, J.-P., & Fort, X. (2004). Compressional salt tectonics (Angolan margin). *Tectonophysics*, *382*(3–4), 129–150. https://doi.org/10.1016/j.tecto.2003.11.014

Brun, J.-P., & Fort, X. (2011). Salt tectonics at passive margins: Geology versus models. *Marine and Petroleum Geology*, *28*(6), 1123–1145. https://doi.org/10.1016/j.marpetgeo.2011.03.004

Callot, J. P., Salel, J. F., Letouzey, J., Daniel, J. M., Mengus, J. M., Pillot, D., & Ringenbach, J. C. (2016). Three-dimensional evolution of salt controlled minibasins: Interactions, folding and megaflap development. *The American Association of Petroleum Geologists Bulletin*, *100*(09), 1419–1442. https://doi.org/10.1306/03101614087

Callot, J. P., Trocmé, V., Letouzey, J., Albouy, E., Jahani, S., & Sherkati, S. (2012). Pre- existing salt structures and the folding of the Zagros Mountains. In G. I. Alsop, S. G. Archer, A. J. Hartley, N. T. Grant, & R. Hodgkinson (Eds.), *Salt tectonics, sediments and prospectivity* (Vol. 363, pp. 545–561). Geological Society. https://doi.org/10.1144/SP363.27

Calvín, P., Casas-Sainz, A. M., Villalaín, J. J., & Moussaid, B. (2018). Extensional vs. compressional deformation in the central high Atlas salt province: A paleomagnetic approach. *Tectonophysics*, *734–735*, 130–147. https://doi.org/10.1016/j.tecto.2018.04.007

Célini, N., Callot, J.-P., Ringenbach, J.-C., & Graham, R. (2020). Jurassic salt tectonics in the SW sub-Alpine fold-and-thrust belt. *Tectonics*, *39*(10), e2020TC006107. https://doi.org/10.1029/2020TC006107

Costa, E., Garcés, M., López-Blanco, M., Beamud, E., Gómez-Paccard, M., & Larrasoaña, J. C. (2010). Closing and continentalization of the South Pyrenean foreland basin (NE Spain): Magnetochronological constraints. *Basin Research*, *22*, 904–917. https://doi.org/10.1111/j.13652117.2009.00452.x

Costa, E., & Vendeville, B. C. (2002). Experimental insights on the geometry and kinematics of fold-and-thrust belts above a weak, viscous evaporite décollement. *Journal of Structural Geology*, *24*(11), 1729–1739. https://doi.org/10.1016/s0191-8141(01)00169-9

Couzens-Schultz, B. A., Vendeville, B. C., & Wiltschko, D. V. (2003). Duplex style and triangle zone formation: Insights from physical modeling. *Journal of Structural Geology*, *25*(10), 1623–1644. https://doi.org/10.1016/s0191-8141(03)00004-x

Curry, M. E., van der Beek, P., Huismans, R. S., Wolf, S. G., Fillon, C., & Muñoz, J. A. (2021). Spatio-temporal patterns of Pyrenean exhumation revealed by inverse thermo-kinematic modeling of a large thermochronologic data set. *Geology*, *49*(6), 738–742. https://doi.org/10.1130/G48687.1

Dahlen, F. A. (1990). Critical taper model of fold-and-thrust belts and accretionary wedges. *Annual Review of Earth and Planetary Sciences*, *18*(1), 55–99. https://doi.org/10.1146/annurev.ea.18.050190.000415

Dahlen, F. A., & Suppe, J. (1988). Mechanics, growth, and erosion of mountain belts. Geological Society of America. *Special Paper*, *218*, 161–178.

Davis, D., Suppe, J., & Dahlen, F. A. (1983). Mechanics of fold-and-thrust belts and accretionary wedges. *Journal of Geophysical Research*, *88*(B12), 1153–1172. https://doi.org/10.1029/jb088ib02p01153

Davis, D. M., & Engelder, T. (1985). The role of salt in fold-and-thrust belts. *Tectonophysics*, *119*(1–4), 67–88. https://doi.org/10.1016/0040-1951(85)90033-2

Davy, P., & Cobbold, P. R. (1991). Experiments on shortening of a 4-layer model of the continental lithosphere. *Tectonophysics*, *188*(1–2), 1–25. https://doi.org/10.1016/0040-1951(91)90311-f

Decker, K., & Peresson, H. (1996). Tertiary kinematics in the Alpine–Carpathian–Pannonian system: Links between thrusting, transform faulting and crustal extension. In G. Wessely & W. Liebl (Eds.), *Oil and gas in Alpidic Thrustbelts and basins of central and eastern Europe* (pp. 69–77). EAGE Special Publication.

Dell'Ertole, D., & Schellart, W. P. (2013). The development of sheath folds in viscously stratified materials in simple shear conditions: An analogue approach. *Journal of Structural Geology*, *56*, 129–141. https://doi.org/10.1016/j.jsg.2013.09.002

Dooley, T. P., Hudec, M. R., Carruthers, D., Jackson, M. P., & Luo, G. (2017). The effects of base-salt relief on salt flow and suprasaltdeformation patterns—Part 1: Flow across simple steps in the base of salt. *Interpretation*, *5*(1), SD1–SD23. https://doi.org/10.1190/INT-2016-0087.1

Dooley, T. P., Hudec, M. R., Pichel, L. M., & Jackson, M. P. (2018). *The impact of base-salt relief on saltflow and suprasalt deformation patterns at the autochthonous, paraautochthonous and allochthonous level: Insights from physical models* (Vol. 476, pp. SP476–13). Geological Society.

Dooley, T. P., Jackson, M. P. A., & Hudec, M. R. (2009). Inflation and deflation of deeply buried salt stocks during lateral shortening. *Journal of Structural Geology*, *31*(6), 582–600. https://doi.org/10.1016/j.jsg.2009.03.013

Duffy, O. B., Dooley, T. P., Hudec, M. R., Fernández, N., Jackson, C. A.-L., & Soto, J. I. (2021). Principles of shortening in salt basins containing isolated minibasins. *Basin Research*, *33*(3), 2089–2117. https://doi.org/10.1111/bre.12550

Duffy, O. B., Dooley, T. P., Hudec, M. R., Jackson, M. P. A., Fernandez, N., Jackson, C. A. L., & Soto, J. I. (2018). Structural evolution of salt-influenced fold-and-thrust belts: A synthesis and new insights from basins containing isolated salt diapirs. *Journal of Structural Geology*, *114*, 206–221. https://doi.org/10.1016/j.jsg.2018.06.024

Duffy, O. B., Fernandez, N., Hudec, M. R., Jackson, M. P. A., Burg, G., Dooley, T. P., & Jackson, C. A. L. (2017). Lateral mobility of minibasins during shortening: Insights from the SE Precaspian basin, Kazakhstan. *Journal of Structural Geology*, *97*, 257–276. https://doi.org/10.1016/j.jsg.2017.02.002

Eichenseer, H. T., Walgengitz, F. R., & Biondi, P. J. (1999). Stratigraphic control on facies and diagenesis of dolomitized oolithic siliciclastic ramp sequences (Pinda Group, Albian, offshore Angola). *AAPG Bulletin*, *83*, 1729–1758.

Eude, A., Roddaz, M., Brichau, S., Brusset, S., Calderón, Y., Baby, P., & Soula, J.-C. (2015). Controls on timing of exhumation and deformation in the northern Peruvian eastern Andean wedge as inferred from low-temperature thermochronology and balanced cross section. *Tectonics*, *34*(4), 715–730. https://doi.org/10.1002/2014TC003641

Ferrer, O. (2012). *Salt tectonics in the parentis basin (eastern Bay of Biscay)* (p. 291). PhD thesis. University of Barcelona.

Ferrer, O., Gratacós, O., Roca, E., & Muñoz, J. A. (2017). Modeling the interaction between presalt seamounts and gravitational failure in salt-bearing passive margins: The Messinian case in the northwestern Mediterranean Basin. *Interpretation*, *5*(1), SD99–SD117. https://doi.org/10.1190/INT-2016-0096.1

Ferrer, O., McClay, K., & Sellier, N. (2016). Influence of fault geometries and mechanical anisotropies on the growth and inversion of hanging-wall synclinal basins: Insights from sandbox models and natural examples. In C. Childs, R. E. Holdsworth, C. A. L. Jackson, T. Manzocchi, J. J. Walsh, & G. Yieldings (Eds.), *The geometry and growth of normal faults* (Vol. 439, pp. 487–509). The Geological Society of London. https://doi.org/10.1144/SP439.8

Ferrer, O., Santolaria, P., Muñoz, J. A., Granado, P., Roca, E., Gratacós, O., & Snidero, M. (2022). Chapter 3: Analogue modelling as a tool to assist seismic structural interpretation in the Andean fold-and-thrust belt. In G. Zamora & A. Mora (Eds.), *Andean structural styles, A seismic Atlas* (pp. 43–61). Elsevier.

Festa, A., Pini, G. A., Dilek, Y., & Codegone, G. (2010). Mélanges and mélange-forming processes: A historical overview and new concepts. *International Geology Review*, *52*(10–12), 1040–1105. https://doi.org/10.1080/00206810903557704

Frisch, W., & Gawlick, H. J. (2003). The nappe structure of the central northern Calcareous Alps and its disintegration during Miocene tectonic extrusion—A contribution to understanding the orogenic evolution of the eastern Alps. *International Journal of Earth Sciences*, *92*(1), 712–727. https://doi.org/10.1007/s00531-003-0357-4

Garcés, M., López-Blanco, M., Valero, L., Beamud, E., Muñoz, J. A., Oliva-Urcia, B., et al. (2020). Paleogeographic and sedimentary evolution of the South Pyrenean foreland basin. *Marine and Petroleum Geology*, *113*, 104105. https://doi.org/10.1016/j.marpetgeo.2019.104105

Ge, H., Jackson, M. P. A., & Vendeville, B. C. (1997). Kinematics and dynamics of salt tectonics driven by progradation. *American Association of Petroleum Geologists Bulletin*, *81*, 398–423.

Ge, Z., Gawthorpe, R. L., Rotevatn, A., Zijerveld, L., Jackson, C. A.-L., & Oluboyo, A. (2020). Minibasin depocentre migration during diachronous salt welding, offshore Angola. *Basin Research*, *32*(5), 875–893. https://doi.org/10.1111/bre.12404

Graham, R., Jackson, M., Pilcher, R., & Kilsdonk, B. (2012). Allochthonous salt in the subAlpine fold–thrust belt of Haute Provence, France. In Salt tectonics, sediments and prospectivity. *Geological Society, London, Special Publications*, *363*(1), 595–615. https://doi.org/10.1144/SP363.30

Granado, P., Ferrer, O., Muñoz, J. A., Thöny, W., & Strauss, P. (2017). Basin inversion in tectonic wedges: Insights from analog modeling and the Alpine-Carpathian fold-and-thrust belt. *Tectonophysics*, *703–704*, 50–68. https://doi.org/10.1016/j.tecto.2017.02.022

Granado, P., Roca, E., Strauss, P., Pelz, K., & Muñoz, J. A. (2019). Structural styles in fold-and-thrust belts involving early salt structures: The Northern Calcareous Alps (Austria). *Geology*, *47*(1), 51–54. https://doi.org/10.1130/g45281.1

Granado, P., Ruh, J. B., Santolaria, P., Strauss, P., & Muñoz, J. A. (2021). Stretching and contraction of extensional basins with pre-rift salt: A numerical modeling approach. *Frontiers of Earth Science*, *9*. https://doi.org/10.3389/feart.2021.648937

Granado, P., Santolaria, P., & Muñoz, J. A. (2022). Interplay of downbuilding and gliding in salt-bearing rifted margins: Insights from analogue modelling and natural case studies. *AAPG Bulletin Special Issue on Salt Basins*. https://doi.org/10.1306/08072221203

Granado, P., Urgeles, R., Sábat, F., Albert-Villanueva, E., Roca, E., Muñoz, J. A., et al. (2016). Geodynamical framework and hydrocarbon plays of a salt giant: The North Western Mediterranean basin. *Petroleum Geoscience*, *22*(4), 309–321. https://doi.org/10.1144/petgeo2015-084

Graveleau, F., Malavieille, J., & Dominguez, S. (2012). Experimental modelling of orogenic wedges: A review. *Tectonophysics*, *538–540*, 1–66. https://doi.org/10.1016/j.tecto.2012.01.027

Grelaud, S., Sassi, W., de Lamotte, D. F., Jaswal, T., & Roure, F. (2002). Kinematics of eastern salt range and south Potwar basin (Pakistan): A new scenario. *Marine and Petroleum Geology*, *19*(9), 1127–1139. https://doi.org/10.1016/S0264-8172(02)00121-6

Hahn, F. F. (1912). Versuch zu einer Gliederung der austroalpinen Masse westlich der österreichischen. *Traun.Verh. k.k. geol. Reichsanst*, *1912/15*, 337–344.

Hahn, F. F. (1913). Grundzüge des Baues der nördlichen Kalkalpen zwischen Inn und Enns. Teil I und II.Mitt. *Geologische Gesellschaft*, *6*(1913), 238–357.

Hearon, T. E., IV., Rowan, M. G., Lawton, T. F., Hannah, P. T., & Giles, K. A. (2015). Geology and tectonics of Neoproterozoic salt diapirs and salt sheets in the eastern Willouran Ranges, South Australia. *Basin Research*, *27*(2), 183–207. https://doi.org/10.1111/bre.12067

Hossack, J. (1995). Geometric rules of section balancing for salt structures. Salt tectonics: A global perspective. *AAPG Memoir*, *65*, 29–40.
Hudec, M. H., & Jackson, M. P. A. (2006). Advance of allochthonous salt sheets in passive margins and orogens. *AAPG Bulletin*, *90*(10), 1535–1564. https://doi.org/10.1306/05080605143
Hudec, M. R., Norton, I. O., Jackson, M. P. A., & Peel, F. J. (2013). Jurassic evolution of the Gulf of Mexico salt basin. *American Association of Petroleum Geologists Bulletin*, *97*, 1683–1710.
Huiqi, L., McClay, K., & Powell, D. (1992). Physical models of thrust wedges. In *Thrust tectonics* (pp. 71–81). Springer.
Izquierdo-Llavall, E., Roca, E., Xie, H., Pla, O., Muñoz, J. A., Rowan, M. G., et al. (2018). Influence of overlapping décollements, syntectonic sedimentation, and structural inheritance in the evolution of a contractional system: The Central Kuqa fold-and-thrust belt (Tian Shan Mountains, NW China). *Tectonics*, *37*(8), 2608–2632. https://doi.org/10.1029/2017tc004928
Jackson, C. A.-L., Jackson, M. P. A., & Hudec, M. R. (2015). Understanding the kinematics of salt-bearing passive margins: A critical test of competing hypotheses for the origin of the Albian Gap. *The Geological Society of America Bulletin*, *127*(11–12), 1730–1751. https://doi.org/10.1130/B31290.1
Jackson, M. P., & Hudec, M. R. (2017). *Salt tectonics: Principles and practice* (p. 498). Cambridge University Press.
Jackson, M. P. A., & Cramez, C. (1989). Seismic recognition of salt welds in salt tectonics regimes, in Gulf of Mexico salt tectonics, associated processes and exploration potential: Society of Economic Paleontologists and Mineralogists Gulf Coast Section. In *10th annual research conference program and abstracts* (pp. 66–71).
Jackson, M. P. A., Dooley, T. P., Hudec, M. R., & McDonnell, A. (2011). The Pillow Fold belt: A key Subsalt structural province in the northern Gulf of Mexico. *AAPG Search and Discovery*, *21*, 10329. http://www.searchanddiscovery.com/pdfz/documents/2011/10329jackson/ndx_jackson.pdf.html
Jackson, M. P. A., Warin, O. N., Woad, G. M., & Hudec, M. R. (2003). Neoproterozoic allochthonous salt tectonics during the Lufilian orogeny in the Katangan Copperbelt, central Africa. *The Geological Society of America Bulletin*, *115*, 314–330. https://doi.org/10.1130/0016-7606(2003)115<0314:nastdt>2.0.co;2
Konstantinovskaya, E., & Malavieille, J. (2011). Thrust wedges with decollement levels and syntectonic erosion: A view from analogue models. *Tectonophysics*, *502*(3–4), 336–350. https://doi.org/10.1016/j.tecto.2011.01.020
Koyi, H. (1988). Experimental modeling of role of gravity and lateral shortening in Zagros mountain belt. *American Association of Petroleum Geologists Bulletin*, *72*, 1381–1394.
Koyi, H., Jenyon, M. K., & Petersen, K. (1993). The effect of basement faulting on diapirism. *Journal of Petroleum Geology*, *16*(3), 285–312. https://doi.org/10.1111/j.1747-5457.1993.tb00339.x
Leitner, C., & Spötl, C. (2017). The eastern Alps: Multistage development of extremely deformed evaporites. In J. I. Soto, J. F. Finch, & G. Tari (Eds.), *Permo-triassic salt provinces of Europe, North Africa and the Atlantic margins* (pp. 467–479). *Tectonics and hydrocarbon potential*. Elsevier.
Letouzey, J., Colletta, B., Vially, R., & Chermette, J. (1995). Evolution of salt-related structures in compressional settings. In: Salt tectonics: A global perspective. *AAPG Memoir*, *65*, 41–60.
Li, J., Webb, A. A. G., Mao, X., Eckhoff, I., Colón, C., Zhang, K., et al. (2014). Active surface salt structures of the Western Kuqa fold–thrust belt, northwestern China. *Geosphere*, *10*(6), 1219–1234. https://doi.org/10.1130/ges01021.1
Linzer, H. G., Moser, F., Nemes, F., Ratschbacher, L., & Sperner, B. (1997). Buildup and dismembering of the eastern Northern Calcareous Alps. *Tectonophysics*, *272*, 97–124. https://doi.org/10.1016/S0040-1951(96)00254-5
Linzer, H. G., Ratscchbacher, L., & Frisch, W. (1995). Transpressional collision structures in the upper crust: The fold-thrust belt of the northern Calcareous Alps. *Tectonophysics*, *242*(1–2), 41–61. https://doi.org/10.1016/0040-1951(94)00152-Y
Lohrmann, J., Kukowski, N., Adam, J., & Oncken, O. (2003). The impact of analogue material properties on the geometry, kinematics and dynamics of convergent sand wedges. *Journal of Structural Geology*, *25*(10), 1691–1711. https://doi.org/10.1016/s0191-8141(03)00005-1
López-Mir, B., Muñoz, J. A., & García-Senz, J. (2014a). Extensional salt tectonics in the partially inverted Cotiella post-rift basin. *International Journal of Earth Sciences*, *104*, 419–434. https://doi.org/10.1007/s00531-014-1091-9
López-Mir, B., Muñoz, J. A., & García-Senz, J. (2014b). Restoration of basins driven by extension and salt tectonics: Example from the Cotiella Basin in the central Pyrenees. *Journal of Structural Geology*, *69*, 147–162. https://doi.org/10.1016/j.jsg.2014.09.022
Malavieille, J., & Konstantinovskaya, E. (2010). Impact of surface processes on the growth of orogenic wedges: Insights from analog models and case studies. *Geotectonics*, *44*(6), 541–558. https://doi.org/10.1134/s0016852110060075
Mandl, G. W. (2000). The Alpine sector of the Tethyan shelf—examples of Triassic to Jurassic sedimentation and deformation from the Northern Calcareous Alps: Mitteilungen der Österreichischen Geologischen Gesellschaft (Vol. *92*, pp. 61–77).
McClay, K., Muñoz, J. A., & García-Senz, J. (2004). Extensional salt tectonics in a contractional orogen: A newly identified tectonic event in the Spanish Pyrenees. *Geology*, *32*(9), 737–740. https://doi.org/10.1130/g20565.1
Moore, V. M., & Blanchard, R. H. (2017). Raft-related structures of the Albian Madiela formation, offshore south Gabon. *AAPG Search and Discovery*, 51373. https://www.searchanddiscovery.com/documents/2017/51373moore/ndx_moore.pdf
Moretti, I., Callot, J.-P., Principaud, M., & Pillot, D. (2013). Salt pillows and localization of early structures: Case study in the Ucayali basin (Peru). *Geological Society, London, Special Publications*, *377*(1), 43–58. https://doi.org/10.1144/sp377.8
Morris, R. G., Sinclair, H. D., & Yelland, A. J. (1998). Exhumation of the Pyrenean orogen: Implications for sediment discharge. *Basin Research*, *10*(1), 69–86. https://doi.org/10.1046/j.1365-2117.1998.00053.x
Mugnier, J. L., Baby, P., Colletta, B., Vinour, P., Bale, P., & Leturmy, P. (1997). Thrust geometry controlled by erosion and sedimentation: A view from analogue models. *Geology*, *25*(5), 427–430. https://doi.org/10.1130/0091-7613(1997)025<0427:tgcbea>2.3.co;2
Muñoz, J. A., Beamud, E., Fernández, O., Arbués, P., Dinarès-Turell, J., & Poblet, J. (2013). The Ainsa fold and thrust oblique zone of the central Pyrenees: Kinematics of a curved contractional system from paleomagnetic and structural data. *Tectonics*, *32*(5), 1142–1175. https://doi.org/10.1002/tect.20070
Muñoz, J. A., Mencos, J., Roca, E., Carrera, N., Gratacos, O., Ferrer, O., & Fernandez, O. (2018). The structure of the South-Central Pyrenean fold and thrust belt as constrained by subsurface data. *Geológica Acta: An International Earth Science Journal*, *16*(4), 439–460. https://doi.org/10.1344/GeologicaActa2018.16.4.7
Nilsen, K. T., Vendeville, B. C., & Johansen, J. T. (1995). Influence of regional tectonics on halokinesis in the Nordkapp Basin, Barents sea. In M. P. A., D. G. Roberts, & S. Snelson (Eds.), *Salt tectonics: A global perspective, 65. AAPG memoir* (pp. 413–436).
Peel, F. J. (2014). The engines of gravity-driven movement on passive margins: Quantifying the relative contribution of spreading vs. gravity sliding mechanisms. *Tectonophysics*, *633*, 126–142. https://doi.org/10.1016/j.tecto.2014.06.023
Peltzer, G., Tapponnier, P., & Cobbold, P. (1982). Les grands décrochements de l'Est Asiatique: Évolution dans le temps et comparaison avec un modèle expérimental. In: Comptes rendus de l'Académie des sciences. Série 2, Mécanique, Physique, Chimie, sciences de l'univers. *Sciences de la Terre*, *294*, 1341–1348.

Peron-Pinvidic, G., & Manatschal, G. (2010). From microcontinents to extensional allochthons. *Witnesses of How Continents Break Apart Petroleum Geoscience*, *16*(3), 189–197. https://doi.org/10.1144/1354-079309-903

Péron-Pinvidic, G., Manatschal, G., & "IMAGinING RIFTING" Workshop Participants (2019). Rifted margins: State of the art and future challenges. *Frontiers of Earth Science*, *7*. https://doi.org/10.3389/feart.2019.00218

Pichel, L. M., Huismans, R. S., Gawthorpe, R., Faleide, J. I., & Theunissen, T. (2022). Late-syn- to post-rift salt tectonics on wide rifted margins—Insights from geodynamic modeling. *Tectonics*, *41*(8), e2021TC007158. https://doi.org/10.1029/2021TC007158

Pichel, L. M., Jackson, C. A.-L., Peel, F., & Ferrer, O. (2021). The Merluza Graben: How a failed spreading center influenced margin structure, and salt deposition and tectonics in the Santos Basin, Brazil. *Tectonics*, *40*(10), e2020TC006640. https://doi.org/10.1029/2020TC006640

Pla, O., Roca, E., Xie, H., Izquierdo-Llavall, E., Muñoz, J. A., Rowan, M. G., et al. (2019). Influence of syntectonic sedimentation and décollement rheology on the geometry and evolution of orogenic wedges: Analog modeling of the Kuqa fold-and-thrust belt (NW China). *Tectonics*, *38*(8), 2727–2755. https://doi.org/10.1029/2018TC005386

Raffel, M., Willert, C. E., Wereley, S., & Kompenhans, J. (2013). *Particle image velocimetry: A practical guide* (p. 255). Springer.

Rasmussen, E. S., Lomholt, S., Andersen, C., & Vejbaek, O. V. (1998). Aspects of the structural evolution of the Lusitanian Basin in Portugal and the shelf and slope area offshore Portugal. *Tectonophysics*, *300*(1–4), 199–225. https://doi.org/10.1016/s0040-1951(98)00241-8

Roca, E., Sans, M., & Koyi, H. A. (2006). Polyphase deformation of diapiric areas in models and in the eastern Prebetics (Spain). *American Association of Petroleum Geologists Bulletin*, *90*(1), 115–136. https://doi.org/10.1306/07260504096

Roma, M., Ferrer, O., McClay, K. R., Muñoz, J. A., Roca, E., Gratacós, O., & Cabello, P. (2018). Weld kinematics of syn-rift salt during basement-involved extension and subsequent inversion: Results from analog models. *Geológica Acta*, *16*(4), 391–410.

Roma, M., Vidal-Royo, O., McClay, K., Ferrer, O., & Muñoz, J. A. (2018). Tectonic inversion of salt-detached ramp-syncline basins as illustrated by analog modeling and kinematic restoration. *Interpretation*, *6*(1), T127–T144. https://doi.org/10.1190/int-2017-0073.1

Rowan, M. G. (2014). Passive-margin salt basins: Hyperextension, evaporite deposition, and salt tectonics. *Basin Research*, *26*(1), 154–182. https://doi.org/10.1111/bre.12043

Rowan, M. G. (2017). An overview of allochthonous salt tectonics. In J. I. Soto, J. F. Flinch, & G. Tari (Eds.), *Permo-triassic salt provinces of Europe, North Africa and the Atlantic margins: Tectonics and hydrocarbon potential* (pp. 97–114). Elsevier.

Rowan, M. G. (2020a). Salt- and shale-detached gravity-driven failure of continental margins. In N. Scarselli, J. Adam, D. Chiarella, D. G. Roberts, & A. W. Bally (Eds.), *Regional geology and tectonics*, *Principles of geologic analysis, Ch.11* (Vol. 1, pp. 205–234). Elsevier. https://doi.org/10.1016/B978-0-444-64134-2.00010-9

Rowan, M. G. (2020b). The South Atlantic and Gulf of Mexico salt basins: Crustal thinning, subsidence and accommodation for salt and presalt strata. *Geological Society, London, Special Publications*, *476*(1), 333–363. https://doi.org/10.1144/sp476.6

Rowan, M. G., & Giles, K. A. (2022). Different scales of salt-sediment interaction during passive diapirism. *AAPG Bulletin Special Issue on Salt Basins*, *105*(1), 53–63. https://doi.org/10.1306/05212020001

Rowan, M. G., Peel, F. J., Vendeville, B. C., & Gaullier, V. (2012). Salt tectonics at passive margins: Geology versus models – Discussion. *Marine and Petroleum Geology*, *37*(1), 184–194. https://doi.org/10.1016/j.marpetgeo.2012.04.007

Rowan, M. G., & Ratliff, R. A. (2012). Cross-section restoration of salt-related deformation: Best practices and potential pitfalls. *Journal of Structural Geology*, *41*, 24–37. https://doi.org/10.1016/j.jsg.2011.12.012

Rowan, M. G., Tilton, J., Lebit, H., & Fiduk, J. A. (2022). Thin-skinned extensional salt tectonics, counterregional faults, and the Albian Gap of Brazil. *Marine and Petroleum Geology*, *137*, 105478. https://doi.org/10.1016/j.marpetgeo.2021.105478

Rowan, M. G., & Vendeville, B. C. (2006). Foldbelts with early salt withdrawal and diapirism: Physical model and examples from the northern Gulf of Mexico and the Flinders Ranges, Australia. *Marine and Petroleum Geology*, *23*(9–10), 871–891. https://doi.org/10.1016/j.marpetgeo.2006.08.003

Rowan, M. G., & Weimer, P. (1998). Salt-sediment interaction, northern green Canyon and Ewing bank (offshore Louisiana), northern Gulf of Mexico. *AAPG Bulletin*, *82*, 1055–1082.

Rushlow, C. R., Barnes, J. B., Ehlers, T. A., & Vergés, J. (2013). Exhumation of the southern Pyrenean fold-thrust belt (Spain) from orogenic growth to decay. *Tectonics*, *32*, 843–860. https://doi.org/10.1002/tect.20030

Santolaria, P., Ferrer, O., Rowan, M. G., Snidero, M., Carrera, N., Granado, P., et al. (2021). Influence of preexisting salt diapirs during thrust wedge evolution and secondary welding: Insights from analog modeling. *Journal of Structural Geology*, *149*, 104374. https://doi.org/10.1016/j.jsg.2021.104374

Santolaria, P., Granado, P., Carrera, N., Schneider, C. L., Ferrer, O., Snidero, M., et al. (2021). From downbuilding to contractional reactivation of salt-sediment systems: Insights from analog modeling. *Tectonophysics*, *918*, 229078. https://doi.org/10.1016/j.tecto.2021.229078

Santolaria, P., Vendeville, B. C., Graveleau, F., Soto, R., & Casas-Sainz, A. M. (2015). Double evaporitic décollements: Influence of pinch-out overlapping in experimental thrust wedges. *Journal of Structural Geology*, *76*, 35–51. https://doi.org/10.1016/j.jsg.2015.04.002

Saura, E., Ardèvol i Oró, L., Teixell, A., & Vergés, J. (2016). Rising and falling diapirs, shifting depocenters, and flap overturning in the Cretaceous Sopeira and Sant Gervàs subbasins (Ribagorça Basin, southern Pyrenees). *Tectonics*, *35*(3), 638–662. https://doi.org/10.1002/2015TC004001

Saura, E., Vergés, J., Martín-Martín, J. D., Messager, G., Moragas, M., Razin, P., et al. (2014). The central high Atlas Jurassic diapiric province: A snapshot of an incipient diapiric passive margin. *Journal of the Geological Society*, *171*(1), 97–105. https://doi.org/10.1144/jgs2013-079

Schellart, W. P. (2000). Shear test results for cohesion and friction coefficients for different granular materials: Scaling implications for their usage in analogue modeling. *Tectonophysics*, *324*(1–2), 1–16. https://doi.org/10.1116/S0040-1951(00)00111-6

Schellart, W. P., & Strak, V. (2016). A review of analogue modelling of geodynamic processes: Approaches, scaling, materials and quantification, with an application to subduction experiments. *Journal of Geodynamics*, *110*, 7–32. https://doi.org/10.1116/j.jog.2016.03.009

Schlunegger, F., & Castelltort, S. (2016). Immediate and delayed signal of slab breakoff in Oligo/Miocene Molasse deposits from the European Alps. *Scientific Reports*, *6*(1), 31010. https://doi.org/10.1038/srep31010

Schnabel, W., Fuchs, G., Matura, A., Bryda, G., Egger, J., Krenmayer, H. G., et al. (2002). *Geologische Karte von Niederösterreich, 3B1*. Vienna, Geological Survey of Austria (GBA), 2 Sheets (scale 1:200,000).

Selley, D., Scott, R., Emsbo, P., Koziy, L., Hitzman, M. W., Bull, S. W., et al. (2018). Structural configuration of the central African Copperbelt: Roles of evaporites in structural evolution, basin Hydrology, and ore location. Society of Economic Geologists, Inc. *SEG Special Publications, no*, *21*, 115–156.

Simpson, G. D. (2006). Modelling interactions between fold–thrust belt deformation, foreland flexure and surface mass transport. *Basin Research*, *18*(2), 125–143. https://doi.org/10.1111/j.1365-2117.2006.00287.x

Sinclair, H. D., Gibson, M., Naylor, M., & Morris, R. G. (2005). Asymmetric growth of the Pyrenees revealed through measurement and modeling of orogenic fluxes. *American Journal of Science*, *305*(5), 369–406. https://doi.org/10.2475/ajs.305.5.369

Snidero, M., Carrera, N., Mencos, J., Butillé, M., Granado, P., Tavani, S., et al. (2020). Diapir kinematics in a multi-layer salt system from the eastern Persian Gulf. *Marine and Petroleum Geology*, *117*, 104402. https://doi.org/10.1016/j.marpetgeo.2020.104402

Snidero, M., Muñoz, J. A., Carrera, N., Butillé, M., Mencos, J., Motamedi, H., et al. (2019). Temporal evolution of the Darmadan salt diapir, eastern Fars region. *Iran. Tectonophysics*, *766*, 115–130. https://doi.org/10.1016/j.tecto.2019.06.006

Stockmal, G. S., Beaumont, C., Nguyen, M., & Lee, B. (2007). Mechanics of thin-skinned fold-and-thrust belts: Insights from numerical models. *Geological Society of America Special Paper*, *433*, 63–98.

Storti, F., & McClay, K. (1995). Influence of syntectonic sedimentation on thrust wedges in analogue models. *Geology*, *23*(11), 999–1002. https://doi.org/10.1130/0091-7613(1995)023<0999:iossot>2.3.co;2

Strauss, P., Granado, P., & Muñoz, J. A. (2020). Subsidence analysis of salt tectonics-driven carbonate minibasins (Northern Calcareous Alps, Austria). *Basin Research*, *33*(2), 968–990. https://doi.org/10.1111/bre.12500

Strauss, P., Granado, P., & Muñoz, J. A. (2021a). Reply to the comment of schollnberger (2021) on "subsidence analysis of salt tectonics-driven carbonate minibasins (Northern Calcareous Alps, Austria)". *Basin Research*, *33*(5), 2636–2642. https://doi.org/10.1111/bre.12577

Strauss, P., Granado, P., & Muñoz, J. A. (2021b). Subsidence analysis of salt tectonics- driven carbonate minibasins (Northern Calcareous Alps, Austria). *Basin Research*, *33*(2), 968–990. https://doi.org/10.1111/bre.12500

Talbot, C. J. (1998). Extrusions of Hormuz salt in Iran. In G. I. Alsop, D. J. Blundell, & I. Davison (Eds.), *Salt tectonics* (Vol. 100, pp. 89–109). Geological Society Special Publications.

Talbot, C. J., Medvedev, S., Alavi, M., Shahrivar, H., & Heidari, E. (2000). Salt extrusion at Kuh-e-Jahani, Iran, from June 1994 to November 1997. In B. Vendeville, Y. Mart, & J.-L. Vigneresse (Eds.), *Salt, shale, and igneous diapirs in and around Europe* (Vol. 174, pp. 93–110). Geological Society Special Publications.

Tapponnier, P., Peltzer, G., Le Dain, A.-Y., Armijo, R., & Cobbold, P. (1982). Propagating extrusion tectonics in Asia: New insights from simple experiments with plasticine. *Geology*, *10*(12), 611–616. https://doi.org/10.1130/0091-7613(1982)10<611:petian>2.0.co;2

Tavani, S., Granado, P., Corradetti, A., Camanni, G., Vignaroli, G., Manatschal, G., et al. (2021). Rift inheritance controls the switch from thin- to thick-skinned thrusting and basal décollement re-localization at the subduction-to-collision transition. *GSA Bulletin*. https://doi.org/10.1130/B35800.1

Tischer, M., Bursik, M. I., & Pitman, E. B. (2001). Kinematics of sand avalanches using particle image velocimetry. *Journal of Sedimentary Research*, *71*, 355–360.

Tollmann, A. (1985). *Geologie von Österreich, Bd. II: Außerzentralalpiner Anteil* (p. 710). Wien (Deuticke).

Tollmann, A. (1987). Late Jurassic/Neocomian gravitational tectonics in the northern Calcareous Alps in Austria. In H. W. Flügel & R. Faupl (Eds.), *Geodynamics of the eastern Alps* (pp. 112–125). Deuticke.

Uranga, R., Ferrer, O., Zamora, G., Muñoz, J. A., & Rowan, M. G. (2022). Salt tectonics of the offshore Tarfaya basin, Moroccan Atlantic margin. *Marine and Petroleum Geology*, *138*, 105521. https://doi.org/10.1016/j.marpetgeo.2021.105521

Vendeville, B. C., Ge, H., & Jackson, M. P. A. (1995). Scale models of salt tectonics during basement-involved extension. *Petroleum Geoscience*, *1*(2), 179–183. https://doi.org/10.1144/petgeo.1.2.179

Vendeville, B. C., & Jackson, M. P. A. (1992). The rise of diapirs during thin-skinned extension. *Marine and Petroleum Geology*, *9*(4), 331–353. https://doi.org/10.1016/0264-8172(92)90047-i

Vendeville, B. C., & Nilsen, K. T. (1995). Episodic growth of salt diapirs driven by horizontal shortening. In C. J. Travis, H. Harrison, M. R. Hudec, B. C. Vendeville, F. J. Peel, & B. F. Perkins (Eds.), *Salt, sediment, and Hydrocarbons. SEPM Gulf Coast section 16th annual research foundation conference* (pp. 285–295).

Vidal-Royo, O., Rowan, M. G., Ferrer, O., Fischer, M. P., Fiduk, J. C., Canova, D. P., et al. (2021). The transition from salt diapir to weld and thrust: Examples from the Northern Flinders Ranges in South Australia. *Basin Research*, *33*(5), 2675–2705. https://doi.org/10.1111/bre.12579

Warren, J. K. (2016). *Evaporites: A geological compendium* (2nd ed.). Springer International Publishing. 1822. https://doi.org/10.1007/978-3-319-13512-0

Warsitzka, M., Kley, J., & Kukowski, N. (2013). Salt diapirism driven by differential loading – Some insights from analog modeling. *Tectonophysics*, *591*, 83–97. https://doi.org/10.1016/j.tecto.2011.11.018

Warsitzka, M., Kley, J., & Kukowski, N. (2015). Analogue experiments of salt flow and pillow growth due to basement faulting and differential loading. *Solid Earth*, *6*(1), 9–31. https://doi.org/10.5194/se-6-9-2015

Warsitzka, M., Závada, P., Jähne-Klingberg, F., & Krzywiec, P. (2021). Contribution of gravity gliding in salt-bearing rift basins – A new experimental setup for simulating salt tectonics under the influence of sub-salt extension and tilting. *Solid Earth*, *12*(8), 1987–2020. https://doi.org/10.5194/se-12-1987-2021

Weijermars, R., Jackson, M. P. A., & Vendeville, B. C. (1993). Rheological and tectonic modeling of salt provinces. *Tectonophysics*, *217*(1–2), 143–174. https://doi.org/10.1016/0040-1951(93)90208-2

Weijermars, R., & Schmeling, H. (1986). Scaling of Newtonian and non-Newtonian fluid dynamics without inertia for quantitative modelling of rock flow due to gravity (including the concept of rheological similarity). *Physics of the Earth and Planetary Interiors*, *43*(4), 316–330. https://doi.org/10.1016/0031-9201(86)90021-x

Wessely, G. (1992). The Calcareous Alps below the Vienna Basin in Austria and their structural and facial development in the AlpineCarpathian border zone. *Geologica Carpathica*, *43*(6), 347–353.

Wessely, G. (2006). *Niederösterreich—Geologie der Österreichischen Bundesländer* (p. 416). Verlag der Geologische Bundesanstalt.

Willet, S. D. (1999). Orogeny and orography: The effects of erosion on the structure of mountain belts. *Journal of Geophysical Research*, *104*(B12), 28957–28981. https://doi.org/10.1029/1999jb900248

Wu, J. E., & McClay, K. R. (2011). Two-dimensional analog modeling of fold and thrust belts: Dynamic interactions with syncontractional sedimentation and erosion. Thrust fault relat. Fold. *AAPG Mem*, *94*, 301–333.

Zamora, G., Carter, B., & Ferrer, O. (2022). Large transport thrust in the Huallaga sub-Basin (northern Peruvian sub-Andean zone). In G. Zamora & A. Mora (Eds.), *Andean structural styles, a seismic Atlas* (pp. 275–284). Elsevier.

Zamora, G., Louterbach, M., & Arriola, P. (2019). Structural controls along the Peruvian subandes. In B. Horton & A. Folguera (Eds.), *Andean tectonics* (pp. 333–362). Elsevier. https://doi.org/10.1016/B978-0-12-816009-1.00015-0